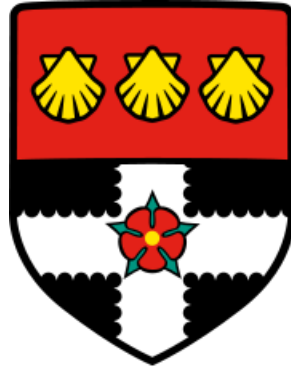UNIVERSITY OF READING

Department of Meteorology

Assessing the simulation of small scale deep convection by high resolution models using a combination of satellite and radar observation data

James Peacock

Abstract

The accurate simulation of small-scale deep convection by numerical weather prediction models is critical to providing forecasts capable of mitigating the impacts of such storms on people, properties and businesses. This is currently a leading problem in the field of meteorology, as existing research identifies numerous inaccuracies in current generation high resolution models. In order to resolve these problems, a complete picture of how simulated storms compare with observed ones is essential.

Combining newly obtained satellite observations with radar measurements, the main objective of this study is to assess and expand upon existing research into the performance of high resolution models when simulating deep convection. A case study of 25th August 2012 was used for analysis of the daytime evolution of the simulated and observed storm properties.

Comparison of statistical analysis has discovered a tendency for the high resolution models studied to produce storms in which the area of deep cloud with cloud tops ≤ 253 K is smaller than the area of precipitation at rates ≥ 4 mm hr^{-1}. The fraction of such rain rates occurring within the deep cloud of simulated storms was found to be increasingly low as resolution increased, with values initially too large at a 1500 m grid length, and an apparent improvement in representation at grid lengths of 500 m and 200 m. The intensity of heavy rain cores at the 1500 m and 500 m grid lengths was observed to be too high when considering an average of storms at each hour, while at 200 m grid length, this analysis has suggested more accurate handling of core intensity. A newly devised method for analysing the complexity of simulated storm structures, by considering their similarity to perfectly spherical storms with rainfall always increasing towards the central point, has revealed that overall, storms are least complex at the 1500 m grid length. However, complexity was seen to increase towards the level seen at 500 m and 200 m grid lengths at several times during the day. This level was close to that calculated from radar data for the majority of the time.

With many problems encountered when attempting to incorporate the satellite observations into the analysis of high resolution models, it was concluded that the relatively low resolution of the data, with a grid length close to 10 km, makes it inadequate for such applications. It is suggested that observations at a much higher resolution are required for this purpose.

Acknowledgements

I would like to thank my supervisors, Dr Robert Plant, Dr Thorwald Stein and Dr Kirsty Hanley, for their support in the production of this dissertation, particularly with regards to the processing and provision of the data used, and the advice given with respect to analysis and interpretation.

Contents

List of Figures

List of Tables

1.   Introduction

Convective storms have contributed to the majority of extreme rainfall events in the UK, for example 30 of the 50 events studied by Hand *et al.* (2004) were predominantly convective, while 15 were frontal and 5 orographic. Precipitation rates are often large enough to generate pluvial flooding within very short timescales (flash flooding from surface water accumulation), which is difficult to predict in any detail. For example, a convergence line over North Cornwall on 16th August 2004 led to intense convective cells training over the region of Boscastle, Cornwall leading to the infamous flood there (Burt, 2005). Two other examples are the very localised Cannington, Somerset flood of 1924, in which a thunderstorm produced a total of 239 mm of rainfall, and the Hampstead, Northwest London flood of 1975, which arose after 171 mm of precipitation fell across just 3 hours (Burt and Lane, 2008). There is also a financial risk from the associated lightning and turbulence, particularly for the aviation industry (Merk and Zinner, 2013). Considering the often extreme nature of these impacts, accurate forecasts for such convective events are highly sought after, and represent a major goal in the field of meteorology.

This can be achieved with the help of accurate high resolution numerical weather prediction model (NWP) simulations. These must correctly represent the mechanisms driving convective storms, which include many dynamical processes occurring on a range of scales. Those on the smaller scales are the most challenging to model, yet continue to be inadequately understood, due in large part to difficulties measuring the mesoscale environment to a high enough resolution (Bennet *et al.*, 2006). Projects such as the Convective Storm Initiation Project (CSIP; Browning *et al.*, 2007) and the Dynamical and Microphysical Evolution of Convective Storms project (DYMECS; Stein *et al.*, 2014) have worked to improve the understanding of these mesoscale processes, and the results are now being applied to model output data to assess their performance and determine where and how improvements can be made. So far this has been carried out using radar observation data, from which a wide range of published results have been obtained. This project aims to expand upon the radar data analysis conducted by Hanley *et al.* (2014), and then apply similar techniques to satellite cloud brightness temperature data.

The main objectives are as follows:

- Determine to what extent statistical analysis using satellite data and model cloud fields does or does not support statistical analysis obtained using radar data.
- Examine the relationship between deep convection and rainfall in the observation data and compare this to that which occurs in the model data, identifying model inaccuracies in the simulation of precipitation, cloud or both.
- Build upon existing methods of analysis using a number of modified or newly constructed approaches.
- Conclude whether the satellite data used provides an effective tool for assessing the performance of models with regards to deep convection.

1.1.   Initiation and Impacts

There are a variety of mechanisms that can initiate convection, usually acting in combination with one another. These occur on a range of spatial and temporal scales, from the large scale movement and interaction of air masses to the small scale perturbation of atmospheric features, these being among the most difficult to accurately model and forecast (Bennet *et al.*, 2006; Browning *et al.*, 2007).

1.1.1.   Boundary Layer Forcing

Wherever heating of the surface terrain occurs, the warming of the near-surface air causes it to rise, and the standard meteorological view is that of air 'parcels' becoming positively buoyant. Such parcels can continue to rise until their temperature falls to that of the surrounding environment, and a further fall in parcel temperature will then cause it to become negatively buoyant, falling back towards the surface. The maximum amount of energy available for air parcels to rise is represented using Convective Available Potential Energy (CAPE), while Convective Inhibition (CIN) represents the energy from external forcing needed to overcome any inversions (temperature increasing with height) to reach the level of free convection (Russell *et al.*, 2008).These can be calculated using equations (1) and (2) respectively, and represented on a tephigram as shown in Figure 1.1. The two equations use standard Meteorological notation; p_0, p_{LFC} and p_{LNB} are the pressure values (hPa) at the surface, the level of free convection and the level of neutral buoyancy respectively. R_d is the gas constant for dry air, while T_p and T_e are the temperatures of the parcel and the environment respectively.

The sum of CAPE and CIN (note that CIN is negative) is proportional to the area between the parcel temperature and the environment curve on the tephigram, and has the units of J kg^{-1}. This definition of CAPE uses parcel theory, which means it assumes that the environment in no way mixes with the ascending parcel, so negating the effects of dry air entrainment and the processes of evaporation and condensation. Pressure gradients arising due to the parcel displacement are also not considered. In reality, these processes do tend to occur, and reduce parcel buoyancy overall, making CAPE an overestimate, but it still serves as a reasonable guide for many meteorological purposes.

$$CAPE = \int_{p_{LFC}}^{p_{LNB}} R_d (T_p - T_e) d\ln p \qquad (1)$$

$$CIN = \int_{p_{LFC}}^{p_0} R_d (T_p - T_e) d\ln p \qquad (2)$$
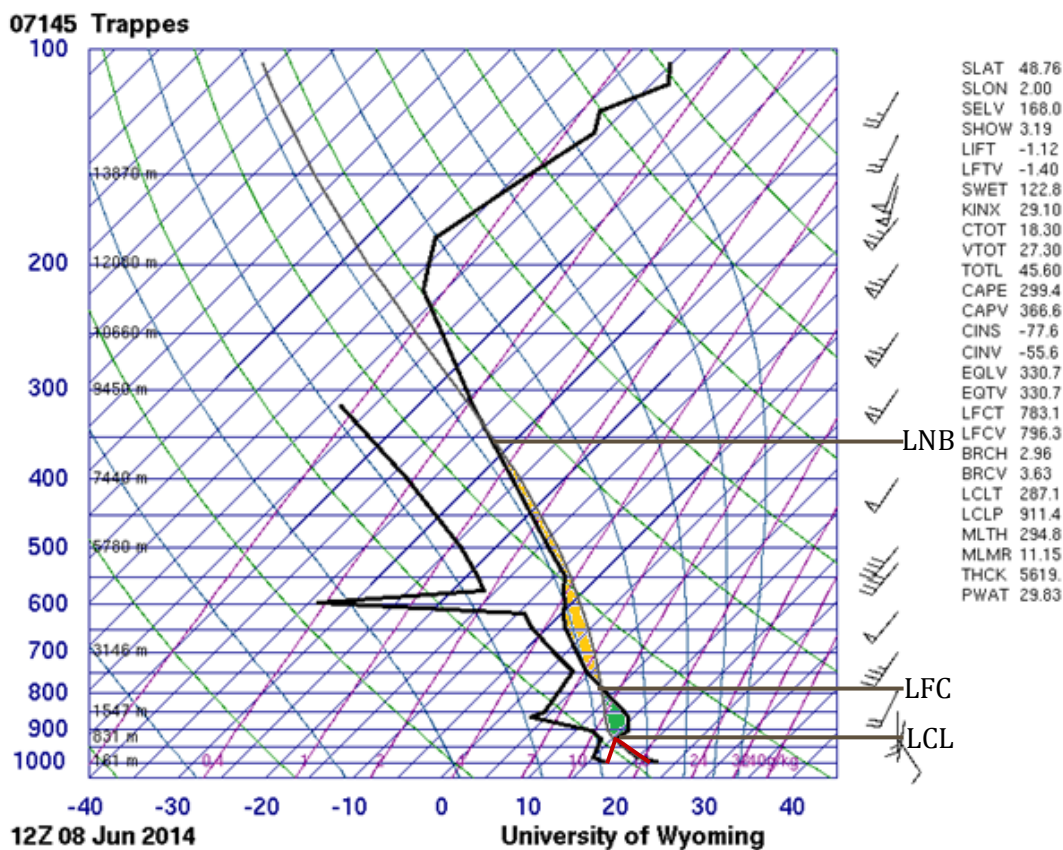
Figure 1.1 ("Atmospheric Soundings", 2014): Example sounding for illustration, valid at 1200 UTC 8th June 2014 for Trappes, North France. CAPE is represented by the area shaded in orange (actual value 299.4 J kg^{-1} K^{-1}) and CIN by the area shaded in green (actual value -77.6 J kg^{-1} K^{-1}). Brown horizontal lines mark the level of neutral buoyancy (LNB), level of free convection (LFC) and lifting condensation level (LCL), the last one determined using Normand's Construction (red lines). The grey line (right-hand edge of the yellow shaded area) is the path theoretically followed by a lifted parcel. The original sounding was modified to add shading and labels.

Within the unsaturated air, 'dry convection' takes place as observed by Battan (1973), and these turbulent motions may be 1-3 km in diameter and hundreds of metres in height, lasting 20-30 minutes. They can either form parallel rows (thermal streets) or be randomly distributed (Hardy and Ottersten, 1969).

If the parcels within the rising thermals become saturated, then the convection produces clouds which can potentially grow to reach the height of the level of neutral buoyancy, though this may be prevented by dry air entrainment. This progression to moist convection often has to overcome a thin 'barrier' within the atmosphere in the form of an inversion. Here, the temperature of the atmosphere increases with height, which tends to make it warmer than that of rising air parcels, resulting in them becoming negatively buoyant. This inversion forms a 'lid' that is often close to the lifting condensation level (LCL), which limits clouds to shallow features. A lid can be broken down by strong thermals having enough momentum to 'punch' through the layer, or by some mesoscale dynamical mechanism that lifts the lid locally, cooling it at the dry adiabatic lapse rate (i.e. rapidly), hence eliminating the associated CIN (Browning *et al*., 2007). Once this occurs, the CAPE, which usually increases markedly during the first part of a day with solar heating, can suddenly be realised at that location, at least in part. This initial 'capping' before a rapid release is important for generating deep convective storms; when CAPE is able to be realised without delay, small, disorganised convection tends to form. This can inhibit further surface heating, or cool the surface and atmosphere beneath the cloud base through evaporative processes, depleting CAPE before it reaches values high enough to support strong storm cells (Bennet *et al*., 2006).

As little as 15hPa of local lid lift (LLL) can initiate deep convection in a maritime climate such as the UK experiences. While the broad-scale potential wet-bulb temperature (θ_w) distribution in the vertical is often used as a good guide for the general regions in which convection can potentially occur, it is the local lifting that tends to determine precisely where the initiation occurs (Browning *et al*., 2007). LLL has long been known to be associated with convergence lines (Purdom, 1982), which arise due to topography, variations in the Bowen Ratio (see references in Weckwerth and Parsons, 2006), or in strong low-level shear environments, convective rolls - parallel lines of convergence separated by regions of divergence (Browning *et al*., 2007). The spatial temperature and humidity variation in the boundary layer, capable of determining whether deep moist convection initiated or not, can be in the order of 1°C and 1gkg[-1] respectively, as observed by Crook (1996). This has long been considered to be on "scales too small to be resolved by conventional observations" (e.g. Weckwerth, 2000), which forms the reasoning behind new methods undertaken in the CSIP (Browning *et al*., 2007) and DYMECS (Stein *et al*. 2014) projects.

1.1.2. Upper-Level Forcing

The principal driving mechanism from the upper levels is the translation of potential vorticity maximums (Browning *et al.*, 2007). On the rear flank of an associated upper level trough, these produce a descent of dry air from the upper troposphere or lower stratosphere. Low θ_w occurs on the underside of this dry air mass, and when this overruns higher θ_w air near the surface, deep convection can be triggered (Browning and Roberts, 1994). It is suggested by Roberts (2000) that this mechanism may be more important than solar heating alone. The overrunning process may be in line with the split-front model of Browning and Monk (1982), in which the leading edge of the dry intrusion (i.e. upper cold front) runs ahead of the surface CF, with a region of convective instability tending to arise in between.

1.1.3. Secondary Generation

The generation of secondary cells is largely down to outflow interactions, with multi-cellular storms a prominent example (Browning, 1978). Interactions can be between storm cells, or with the broad-scale airflow (ambient conditions).

Storm cells feature downdrafts of relatively cool air, and as these reach the surface terrain, they are forced to spread out and travel horizontally, forming an outflow boundary, sometimes called a gust front. Where this travels against the ambient airflow, near-vertical upward motion is induced as the colder outflow undercuts the warmer air that it meets, behaving much like a gravity wave in this sense (Morcette *et al.*, 2006; Marsham and Parker, 2006). This can generate storm cells, particularly if the upper level wind is in the direction of the outflow. When the ambient flow is with the outflow direction, and the upper level flow against it, the updraft tends to be very tilted and disperses in the higher level airflow, limiting convective potential (Garner and Thorpe, 1992). Browning *et al.* (2007) observed this process occurring at 2pm on 25th August 2005, with an arc of convection initiating along a gust front containing air some 8°C cooler than that ahead of it.

1.2.   Case Study: 25th August 2012

1.2.1.   The Large Scale Situation

A trough of low pressure was located over the United Kingdom on 25th August 2012, with a minimum pressure of 998mb at 1200 UTC (Figure 1.2B). Associated with this system is an occluded front which wraps around the observation region, implying a mature low pressure system, with the increasingly less defined warm sector covering the area. Within this, a trough line suggests an atmospheric perturbation that could have served as a focus for convective storms to develop in an organised manner.

This system had changed little in position and intensity since the beginning of the day (Figure 1.2A), but by the start of 26th August 2012, it had shifted further east and into the North Sea while continuing to weaken (not shown). The implication is that the unstable airmass associated with it progressed in a similar fashion, resulting in the most unstable conditions progressing eastward during the middle part of the day across the observation area.

(A)   (B)
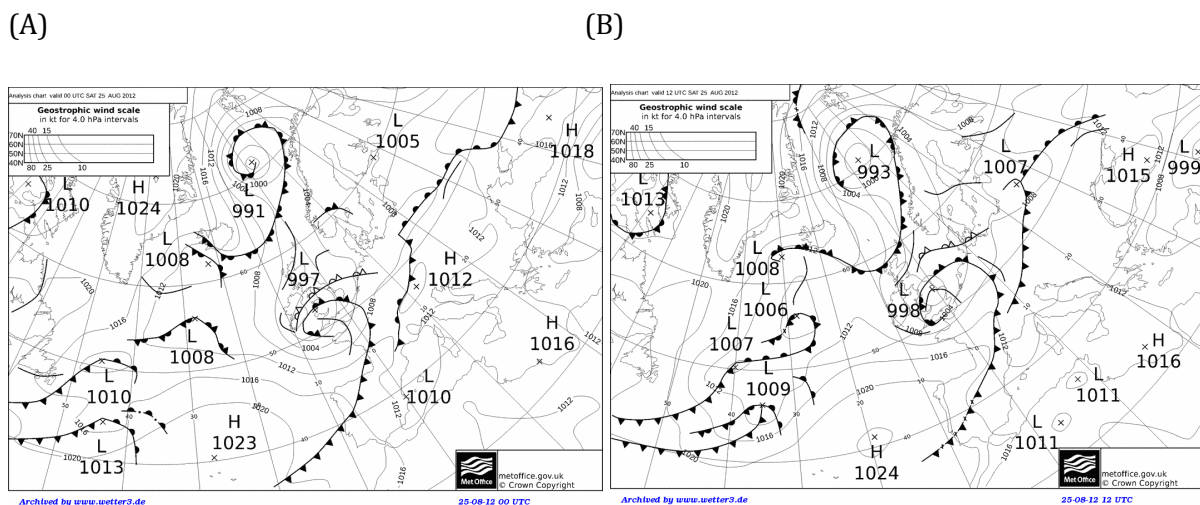
Figure 1.2: Met Office synoptic analysis charts for A) 0000 UTC 25th August 2012 and B) 1200 UTC 25th August 2012.

1.2.2.   Air Mass Analysis

A reasonable guide to the nature of the air mass across the region is the progression of 850hPa temperatures leading up to 25th August 2012, with the chart for 1200 UTC on that day (Figure 1.3) revealing the warm sector contained within the wrapped around occlusion (visible in Figures 1.2A and 1.2B), positioned over the observation region. At 8-9 °C, this air mass is fairly

typical of a warm sector within a low pressure system across the UK in late August. The preceding charts (not shown) reveal that the warm sector air mass originated in the western North Atlantic, at a similar latitude to the UK, approximately south of Greenland.

The sounding at 0900 UTC for Larkhill in southern England (Figure 1.5) shows a number of features that indicate an environment conducive for convection to initiate. Surface heating has resulted in the atmospheric temperature (right-hand solid black line) cooling faster than the dry adiabatic lapse rate (solid red line) across the lowest 300 m or so of the atmosphere, and then close to that rate up to the LCL. This means that a parcel can easily become buoyant and remain so to the level where it becomes saturated and contributes to the formation of convective clouds. Above this level, the atmosphere cools at a rate close to, but often slightly faster than, the moist adiabatic lapse rate that a rising parcel follows (red dashed line). This means that parcels can potentially remain buoyant right up to the LNB (indicated by the CAPE present, shaded in yellow and reported to be 142.4 J kg^{-1} at the time of observation), perhaps overshooting this level if they have enough inertia. This indicates the possibility of convective clouds reaching between 9 and 10 km above the surface.

Observed conditions across the study region support these deductions (Table 1.0), and reveal that further surface heating occurred not far from Larkhill up to around 2pm BST, after which time thunderstorms affected the area. Increasing the surface temperature to 21°C, matching the Farnborough observations, while assuming little change in the surface dew point temperature or atmospheric temperatures above, it is possible to visualise a large increase in CAPE at Larkhill. The Atlantic and Europe CAPE reanalysis chart values for noon of 300-900 J kg^{-1} CAPE and Lifted Index values of -2 (Figure 1.4) reveal that CAPE increased substantially in the region of Larkhill during the preceding three hours. A similar evolution on the broader scale is seen to have created a very favourable vertical profile across the whole western half of the region, and subsequent charts imply that this translated east during the afternoon (not shown).

The observation data in Table 1.1 reveals dew points of 14 to 16 °C, indicating moist surface air which is a key ingredient for allowing convection to develop from initial cumulus clouds to cumulus congestus clouds, and finally cumulonimbus clouds, as moisture is lifted through the atmosphere and works to mix out any drier air aloft. The 3:20 PM and 3:50 PM observations reveal this process to have resulted in a thunderstorm or two over Farnborough.

The combination of all these statistics constructs a scenario of deep convection initiating across much of England during the day of study, occurring during the morning across the western half of the study region, and extending to the whole region by around 1500 UTC.
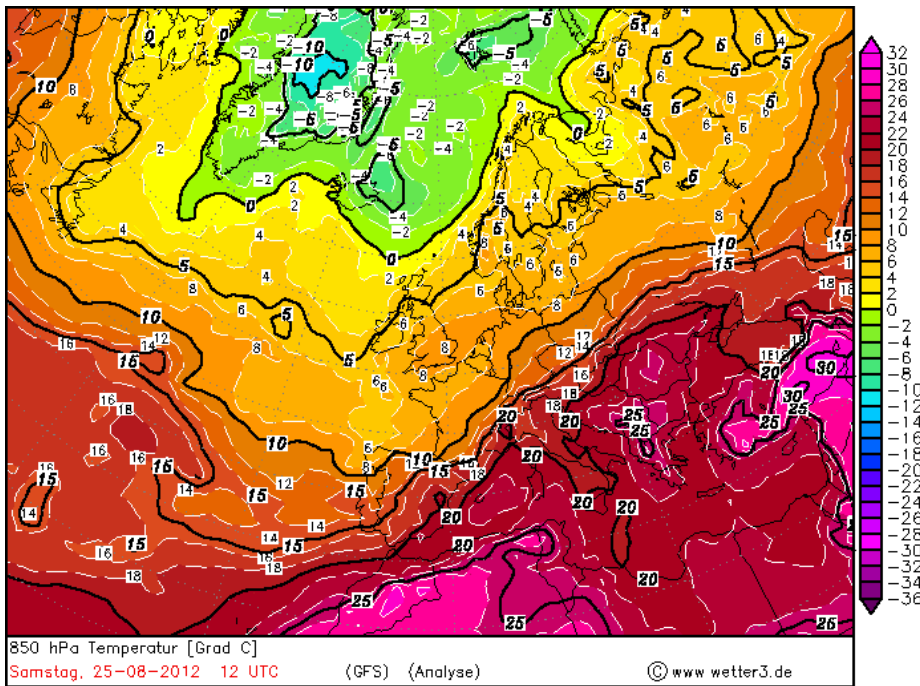
Figure 1.3 ("Archiv-Version des Animationstools", 2014): 850hPa reanalysis chart for 1200 UTC 25th August 2012.
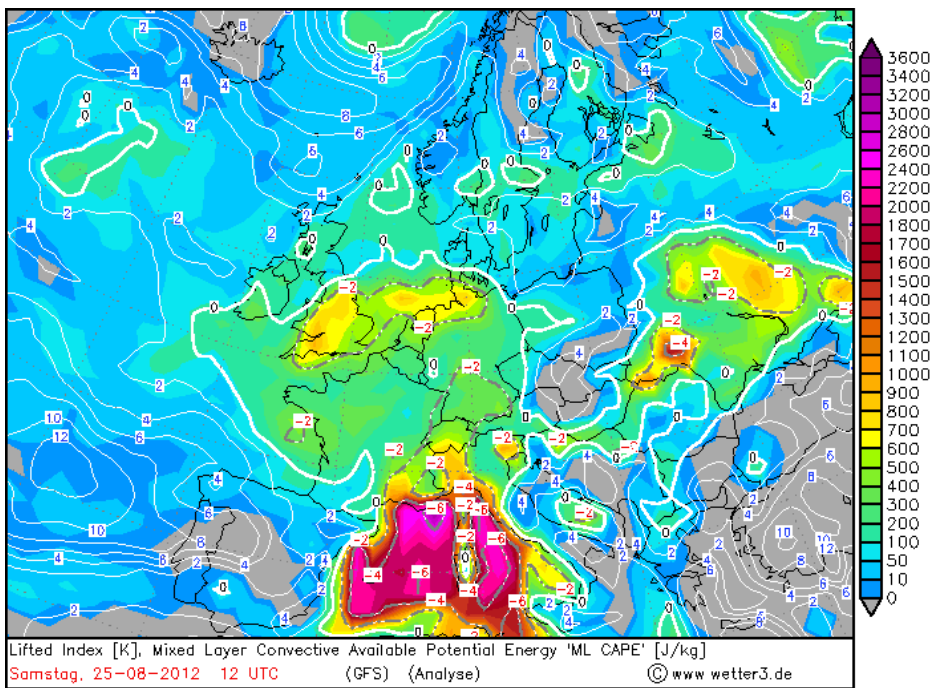
Figure 1.4 ("Archiv-Version des Animationstools", 2014): CAPE reanalysis chart for 1200 UTC 25th August 2012.

03743 Larkhill

SLAT 51.20
SLON -1.80
SELV 133.0
SHOW -0.61
LIFT -1.62
LFTV -1.84
SWET 221.6
KINX 26.10
CTOT 26.30
VTOT 27.30
TOTL 53.60
CAPE 142.4
CAPV 207.5
CINS -0.22
CINV -0.12
EQLV 341.2
EQTV 340.0
LFCT 920.3
LFCV 922.2
BRCH 17.20
BRCV 25.05
LCLT 284.8
LCLP 931.0
MLTH 290.7
MLMR 9.38
THCK 5532.
PWAT 22.25

LNB
LFC
LCL
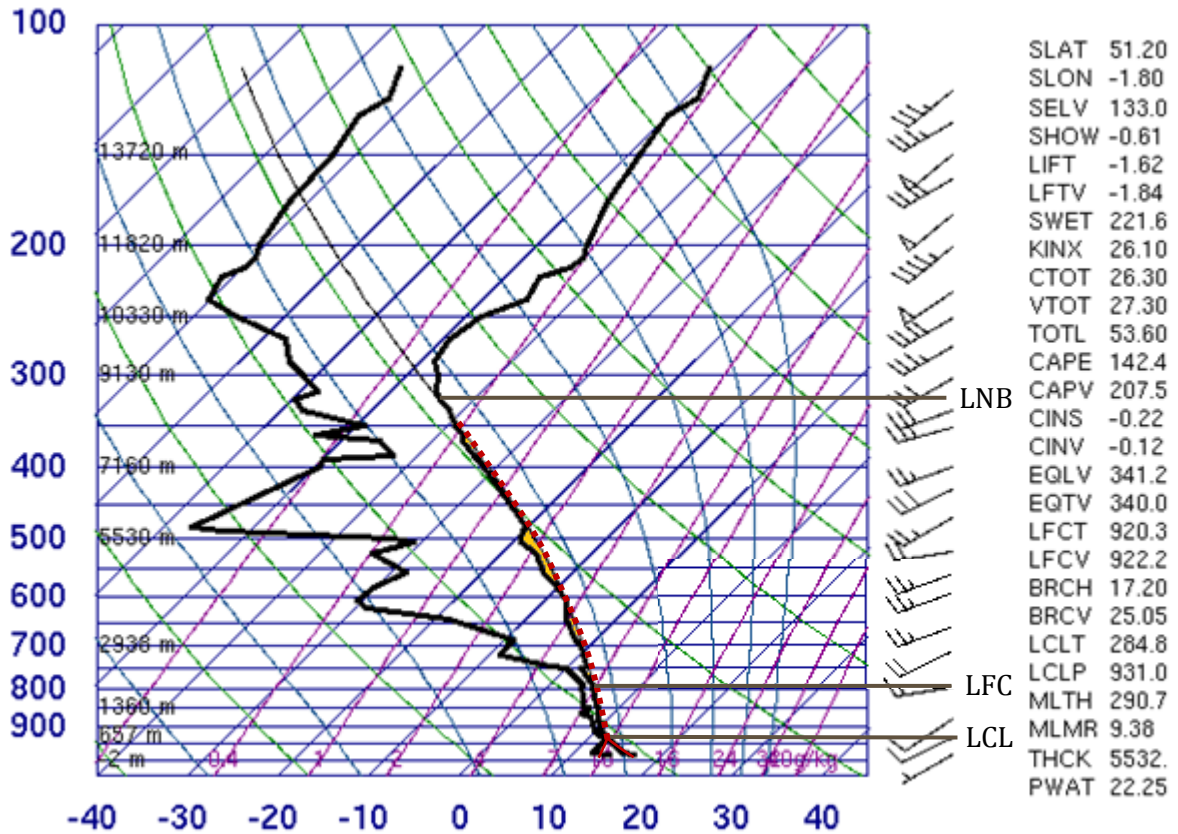
09Z 25 Aug 2012 — University of Wyoming

Figure 1.5 ("Atmospheric Soundings", 2014): Sounding for Larkhill, southern England at 0900 25th August 2012. The original sounding was modified to add shading and labels in the same way as in Figure 1.1, followed by the addition of a dotted red line to make the lifted parcel path clearer to see.

Table 1.1 ("Farnborough Hourly Weather History and Observations", 2014): Observation data for Farnborough, Southern England on 25th August 2012 (the nearest available location to Larkhill).

Hourly Weather History & Observations

Time [BST]	Temp.	Dew Point	Humidity	Pressure	Visibility	Wind Dir	Wind Speed	Gust Speed	Precip	Events	Conditions
10:50 AM	18.0 °C	15.0 °C	83%	1000 hPa	10.0 km	SW	18.5 km/h / 5.1 m/s	-	N/A		Scattered Clouds
11:20 AM	19.0 °C	14.0 °C	73%	1000 hPa	10.0 km	WSW	24.1 km/h / 6.7 m/s	-	N/A		Scattered Clouds
11:50 AM	19.0 °C	14.0 °C	73%	1000 hPa	10.0 km	WSW	20.4 km/h / 5.7 m/s	-	N/A		Scattered Clouds
12:20 PM	20.0 °C	14.0 °C	68%	1000 hPa	10.0 km	SW	24.1 km/h / 6.7 m/s	-	N/A		Scattered Clouds
12:50 PM	20.0 °C	14.0 °C	68%	1000 hPa	10.0 km	SW	25.9 km/h / 7.2 m/s	-	N/A		Scattered Clouds
1:20 PM	19.0 °C	14.0 °C	73%	1000 hPa	10.0 km	SW	31.5 km/h / 8.7 m/s	-	N/A		Scattered Clouds
1:50 PM	20.0 °C	14.0 °C	68%	1000 hPa	10.0 km	SW	29.6 km/h / 8.2 m/s	-	N/A		Scattered Clouds
2:20 PM	21.0 °C	14.0 °C	64%	1001 hPa	10.0 km	SW	29.6 km/h / 8.2 m/s	-	N/A		Scattered Clouds
2:50 PM	19.0 °C	15.0 °C	78%	1001 hPa	10.0 km	SSW	24.1 km/h / 6.7 m/s	-	N/A	Thunderstorm	Scattered Clouds
3:20 PM	17.0 °C	16.0 °C	94%	1001 hPa	4.0 km	SSW	20.4 km/h / 5.7 m/s	-	N/A	Rain , Thunderstorm	Thunderstorms and Rain
3:50 PM	16 °C	14 °C	88%	1002 hPa	11 km	SW	18.5 km/h /	-	-		Mostly Cloudy
3:50 PM	15.0 °C	14.0 °C	94%	1002 hPa	10.0 km	SSW	18.5 km/h / 5.1 m/s	-	N/A	Rain , Thunderstorm	Thunderstorms and Rain
4:20 PM	17.0 °C	15.0 °C	88%	1002 hPa	10.0 km	SSW	20.4 km/h / 5.7 m/s	-	N/A		Scattered Clouds

1.3.　　　　High Resolution Modelling of Convective Storms

In light of the potentially severe impacts of convective storms outlined in Section 1, it is highly desirable to model convection as accurately as possible, so that forecasts, warnings and guidance may be effectively issued. A widely investigated approach to improving the accuracy of model simulations is to reduce the size of the grid boxes within a model, increasing resolution.

An increase of model resolution from a 12 km grid length to a 4 km grid length or less enables dynamical representation of more and smaller scale features, with more than one grid box covering each convective cell (Figure 1.6). This allows for explicit representation of convection as opposed to using parameterisation (Lean *et al*., 2008). This approach, running order 1 km grid-length models, has been undertaken by many organisations for short range weather forecasting, including the Met Office (Lean *et al*., 2008). Numerous studies (Weisman *et al*., 1997; Romero *et al*., 2001; Speer and Leslie, 2002; Done *et al*., 2004) demonstrate improved thunderstorm representation along with squall lines and others, as the grid length reduced towards 1 km. On the other hand, Bryan and Rotunno (2005) and Petch (2006) show evidence that, as of 2005-2006, convection was seriously under-resolved at 4 km, and to a lesser extent at 1 km. Hanley *et al*. (2014) suggest that this remains the case as of early 2014. From experiments using a 4 km model, Lean *et al*. (2008) observed that simulated rain rates were generally higher than in observation data, and by an amount that may be proportional to the overall rain rate. A possible inherent predisposition towards overdoing rain rates is suggested, arising from convection being under-resolved. From this and other results, Lean *et al*. (2008) go on to express an opinion that it is undesirable to model convective cells smaller than around 12-16 km in diameter, due to the likelihood of numerical inaccuracy.

These shortcomings manifest themselves in significant ways in the modelling of convective storms. As an example, the Met Office's current operational 1.5 km grid-length UK model tends to produce oversized storms with an excess of heavy rain and deficit of light rain (e.g. McBeath *et al*., 2014). On top of this, mesoscale complexes observed in reality are often not developed by the model, the organising processes seemingly underdone or missed as a result of microphysical processes not being fully or accurately simulated (Hanley *et al*., 2014).
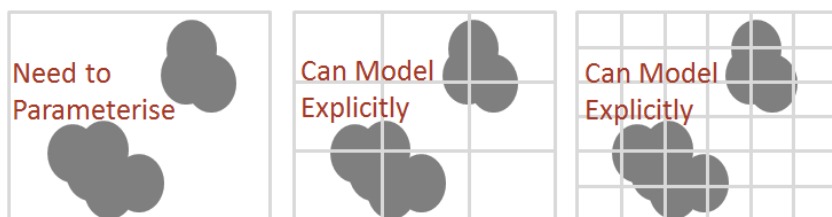

Figure 1.6: schematic illustrating the effect of reducing grid length. This can result in a convective cell covering multiple grid boxes, making explicit representation in a NWP model more effective.

1.4.　　　　Observing Convection Using Satellite Imagery

While radar observations have often been used as a standalone data source for assessing the accuracy of model simulations, there are far fewer cases in that have combined them with ones made by satellite. Among the earliest examples is a study by Houze and Rappaport (1984), in which the life cycle of as squall line off the coast of Africa is characterised through joint analysis of geostationary infra-red satellite imagery and three-dimensional ship radar data. The region of study was chosen for the typically very large, deep storms that are common there. This is due to the fact that satellite observations are of relatively low resolution, unable to pick out smaller scale features, particularly as higher latitudes including Europe (Merk and Zinner, 2013). The same reasoning is outlined in a recent study by Futyan and Genio (2007), who made 'insightful' observations using a range of satellite products, including the Microwave Imager (TMI) and Lightning Imager Sensor (LIS).

Satellite observations are also subject to a number of limitations and uncertainties, making them undesirable for some applications. In particular, low cloud brightness temperatures can be measured from thin cirrus clouds advecting over cumulus clouds, giving the impression that the cumulus cloud tops are growing colder, when this is not actually the case (Merk and Zinner, 2013). Observations of cloud tops are also impacted by the oblique viewing angle at higher latitudes, as information from the sides of clouds influences the measured signal (Merk and Zinner, 2013).

The question as to whether satellite observations at their current resolution (close to 10 km for the UK) can provide observations of much use in climates such as that of the United Kingdom, with relatively small scale convection, will be explored in this study.

1.5.　　　　Summary

An insufficient ability to accurately model deep convection, a large contributor to severe rainfall events in the UK, has driven extensive research into such storms, and observation of them on the mesoscale using radar equipment. The resulting data has been compared with predicted fields from models with grid lengths as low as 200 m, and it has become apparent that the models display erroneous behaviour of varying nature as grid length is reduced. Examining a case study in which deep convection developed widely across Central Southern England, this project aims to expand upon the radar composite analysis of Hanley *et al*. (2014), and then use satellite data to both reinforce existing findings and carry out new forms of analysis, further investigating how the model simulations compare with the observations that day. The effectiveness of using satellite observations will be assessed based on the results.

2.   Model Configuration

This chapter outlines the properties of the models used in this study. It begins by introducing the Met Office Unified Model (UM), which provides the data for analysis. The various configurations of the model used to investigate the effects of changing resolution are then described. The chapter closes with a consideration of model limitations and uncertainties.

2.1.   The Met Office Unified Model

This study works with the Met Office Unified Model (UM) version 7.8, an operational numerical weather prediction model that is used to provide deterministic and ensemble forecasts both globally and regionally. A semi-implicit, semi-Langrangian numerical scheme is used to solve non-hydrostatic, deep-atmosphere dynamics (Cullen *et al.*, 1997; Davies *et al.*, 2005). Arakawa C staggering is used in the horizontal, and Charney-Phillips staggering in the vertical. The grid is regular latitude-longitude, but for limited area model configurations, the pole of the grid is rotated in order to approximately centre the domain on the equator, so minimising changes in grid-length across the domain. Four separate schemes handle the surface layer (Best *et al.*, 2014), radiation (Edwards and Slingo, 1996), mixed-phase cloud microphysics (Wilson and Ballard, 1999) and non-local boundary layer (Lock *et al.*, 2000).

The model stops using a convective parameterisation scheme at grid lengths of 1.5 km and below. Resolutions of length close to 1 km use a sub-grid turbulence scheme, similar in nature to those often used for large-eddy simulation. It is a first-order closure scheme based on Smagorinsky (1963) as detailed in Halliwell (2007), using an eddy viscosity coefficient calculated from variables such as the mixing length. It can be applied in just the horizontal, or coupled with the vertical, as is the case for the 500 m and 200 m models used in this study. In the latter case, the non-local boundary layer (BL) scheme is deactivated and the local BL scheme uses diffusion coefficients calculated from the sub-grid turbulence scheme.

2.2.   Model Configurations

The Met Office deterministic operational nested suite was made up of four configurations as of 25th August 2012. These were the Global, North Atlantic and European (NAE), UK 4 km (UK4) and UK Variable-Resolution (UKV) configurations. Nested within the global model (25 km grid length), the UKV model is a limited-area version of the UM, and consists of both inner (shown in Figure 2.1) and outer areas at 1.5 km and 4 km resolution respectively, plus a transition region. In the vertical, there are 70 levels in the UKV model, at a spacing which increases quadratically with height up to the top of the domain at 40 km. For each run of the UKV model (with

initialisation times, T, of 0300, 0900, 1500 and 2100 UTC each day), initial and boundary data are sourced from the Global run initialised 3 hours prior. There is a data assimilation process from (T-2) to (T+1) hours, for fields including surface and satellite-derived 3D cloud fractions and radar-derived surface rain rates.

The models used for data in this study are one-way nested models with grid lengths of 1500 m, 500 m (domain size 500 x 425 km) and 200 m (domain size 300 x 225 km) (Figure 2.1). They all treat convection explicitly. Initial conditions for the 1500 m and 500 m models are the output of the assimilation cycle described earlier, while the 200 m model gets initial conditions from the 500 m model, within which it is nested. Lateral boundary conditions for the 1500 m model were obtained from the 0000 UTC NAE forecast, while the 500 m model gets conditions from the 1500 m run, and the 200 m model from the 500 m run. The 200 m initialisation time is 3 hours later than the other models, to allow the 500 m model the time needed for the higher-resolution convective features to be developed having been absent in the initial condition data (this is the 'spin-up' time). This setup is as used by Hanley *et al.* (2014), with a UKV setup matching that which was operational at the beginning of DYMECS (summer 2011), and the 500 m and 200 m models configured along the lines of high-resolution UM simulations performed by Vosper *et al.* (2013). They feature twice the number of vertical levels in the UKV model, and differences in the critical relative humidity level used to assume that a grid box does or does not contain some cloud (Vosper *et al.*, 2013). Runs are analysed from 1000 UTC onward, as simulated and observed convection was limited in presence before that time.
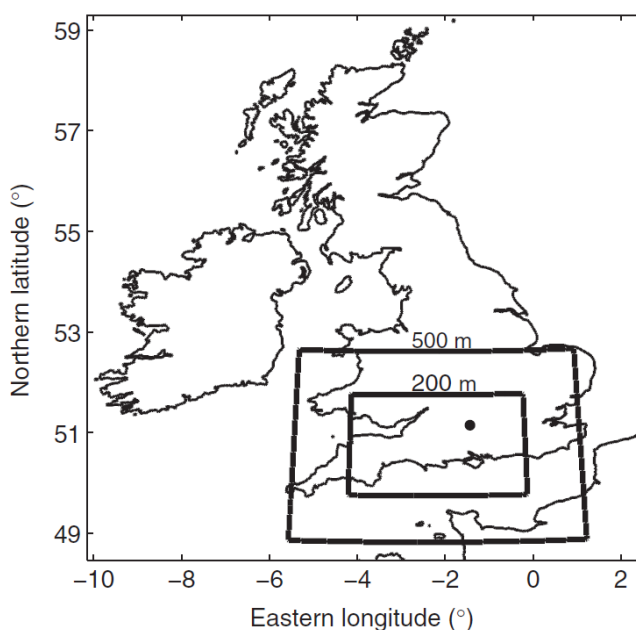
Figure 2.1 (Hanley *et al.*, 2014): the domains of the three models used, the outermost being the fixed-length part of the UKV (1500 m grid length), the inner two being the nested higher resolution models. The black dot indicates the position of the Chilbolton radar.

2.3.   Model Limitations and Uncertainty

Prediction has a fundamental limit for small-scale structures (Lorenz, 1969; Hohenegger and Schar, 2007); it is highly unlikely that every individual cell in a region of convection will be predicted correctly. This is a key point to convey to customers (Roberts and Lean, 2008). When analysing fields of predicted convection, this study therefore focuses on the general morphology of the convective storms, as opposed to their locations relative to observed storms. The uncertainties in storm structure ultimately depend on the observation data that is used to construct the initial conditions. This uncertainty can be mitigated through the use of data from the simulation of large numbers of storms, taken at small time intervals across a large number of hours.

3.   Methodology

The approaches used to obtain the observation data against which to compare the model fields are outlined in the first section of this chapter. The proceeding section then details the data analysis process carried out and the methods used to compare the different datasets.

3.1.   Observation Data

For precipitation data, this project uses the Met Office radar rainfall composite observation data for 25th August 2012. Estimated from the Met Office network of C-band radars, the rainfall observations were regularly calibrated to rain gauge data (Harrison *et al.*, 2011). The reflectivity data from the each radar is composed of 5-minute scan sequences of four elevations from the 15 C-band radars across the UK, at a resolution of 600 m in range and 1° in azimuth. From the single-polarisation radar data, the Marshall *et al.* (1955) empirical relationship for mid-latitude stratiform rain is used to estimate rainfall rates (Harrison *et al.*, 2011):

$$Z = 200\, R^{1.6} \quad (3)$$

where Z is the radar reflectivity ($mm^6\, m^{-3}$) and R is the rainfall rate ($mm\, h^{-1}$).

A quality control procedure is applied to the rainfall estimation which includes noise filtering, cluster identification and beam blockage (Harrison *et al.*, 2009). Rainfall rate attenuation (A, in dB) is achieved using the Gunn and East (1954) relationship:

$$A = 0.0044\, R^{1.17}\ (4)$$

which may correct by up to a factor of 2 in the rainfall rate. The vertical profile of reflectivity is parameterized, including bright band and orographic growth, to simulate the equivalent radar reflectivity close to the ground, which is then input to equation (4) to estimate the surface rainfall rate (Harrison *et al.*, 2009). This form of attenuation corrected relationship is shown by Bringi *et al.* (2011) to have a mean absolute error of 31 % for rain rates above 3 mm h^{-1} when compared to hourly rain gauge observations.

For satellite data on the same date, this project uses observations made by the Meteosat Spinning Enhanced Visible and Infra-Red Imager (SEVIRI). With 12 different available channels, the images refresh every 15 minutes in normal scan mode and every 5 in rapid scan mode (Merk and Zinner, 2013). This project performs analysis using the cloud brightness temperature (CBT) data (the temperature corresponding to the amount of reflected infra-red radiation detected by the instrument), which from this point forward is referred to as the satellite data.

3.2.　　Data Analysis and Comparison

3.2.1.　　Labelling Storms

In order to restrict the data analysis to regions of deep convection, excluding precipitation and CBT data from shallow convection and stratiform cloud formations, a storm labelling process was used. This applies the *local table method* as detailed by Haralick and Shapiro (1992). For each radar image, all pixels in which the rain rate or cloud temperature meet or cross a given threshold are labelled, producing a matrix of values. Then, for each line in turn, each new labelled region is compared with those of the previous line to see if it is adjacent to one or more of them (the equivalence method). The lowest label value among adjacent regions is then assigned to the new combined region. In the case of multiple adjacent regions, the equivalence method is carried out twice more, first right to left and then bottom to top across the matrix.

The threshold for CBT chosen for this study is 253 K, as this corresponds to a cloud depth of close to 5 km in the Larkhill sounding (Figure 1.5), which is considered deep by UK standards. Restricting radar composite and model rain rate data to the heavier rain rates that tend to be associated with deep convection was achieved using a threshold of 4 mm hr^{-1}, as this produced the best coverage of deep cloud identified (see Figure 4.3D) without restricting the amount of labelled data too far.

3.2.2.　　Radar Composite and Model Rain Rate Data　Analysis

Initially, similar analysis was carried out to that of Hanley *et al*. (2014), in which the same case study was examined. The purpose was to ensure that the data could be further analysed in light of the existing results, using time series plots to compare the evolution of convective storms in each dataset with those presented in the paper.

Having identified no problems with the radar composite and model rain rate datasets (referred to as the rain data from this point forward), they were used to create frequency distributions at hourly intervals, spanning the duration of the model run starting at 1000 UTC, or in the case of the radar composite data, using data from 1000 UTC to 2200 UTC to match the timespan of the 1500 m model. This was carried out for the mean storm equivalent diameters (SED), and the mean storm rainfall rates. The former considers a circle with the same area as the storm, and the value is the diameter of that circle in kilometres, used for easier visualisation of what the data represents.

The frequency distributions derived from rainfall data were then compiled into diagrams of distribution evolution over time. To account for differences in bin widths, the magnitudes were grouped into three categories; small (3-10 km), medium (10-15 km) and large (15-20 km) for the SED, and light (4-6 mm hr^{-1}), moderate (6-12 mm hr^{-1}) and heavy (12-30 mm hr^{-1}) for the rainfall rates. This also allowed for a more intuitive interpretation of what the diagrams displayed in terms of the distribution of storms through the day. Due to large differences between the number of storms detected in the radar composite data and each of the models, the data was normalised to allow for effective cross-comparison of the distributions.

To obtain a measure of how close the observed and modelled storm cells are to circular blobs, referred to from this point forward as the 'Blob Factor', the location of the maximum rain rate relative to each storm cell was determined. To allow for analysis at half-hourly intervals without unreasonable computing time, the centre of each labelled storm was represented by the centroid position of an associated smallest enclosing circle. The co-ordinate position of this on the grid was then compared with that of the maximum rainfall rate for the storm, and Pythagoras Theorem applied to determine the scalar distance between the points (in km). To account for variation in SED between the models, this scalar distance was then divided by the equivalent diameter for the storm, producing a proportional value. This is the 'Blob Factor' value for the storm, and once all storms for a given timeframe had been analysed in this way, a mean proportion was calculated. Through this method, time series of mean 'Blob Factors' were generated for the radar composite and each of the three models.

The centroid values are used because they represent where the maximum rain rate would occur in perfectly spherical storms with rain rates steadily increasing from the edge towards a peak in the middle; storms close to this form would appear in rainfall fields as a single blob. It is hypothesised that storms with a more complex structure arising from higher resolution modelling are more likely to feature peak rain rates located further away from the centroid position. The more irregular patterns in rain rate have less of a blob-like appearance. It is likely that some storms will still have small centroid-max rain rate differences, but these are expected to make up the minority of cases. Based on the output from this planned 'Blob Factor' analysis, potential relationships with other variables were investigated using scatter plots.

3.2.3.   Matching Radar Composite Data With Satellite Data

To establish that the radar composite and satellite data could be related to one another and hence used in combination for analysis, contour plots of rainfall equal to or greater than a 4 mm hr^{-1} threshold were overlaid with contour plots for cloud temperatures equal to or lower than a 253 K threshold for the associated time of day. Due to the fact that a scan using SEVIRI takes a

number of minutes to cover the region of the United Kingdom, the radar data from 4 minutes after the satellite scan initiation time was used in each case. A more significant adjustment was made to the satellite data to account for parallax (Vincente *et al.*, 2002).

3.2.4. Satellite Data Analysis and Comparison with Radar Composite Results

The process for creating frequency distributions, their evolution through time, and model errors was repeated using the satellite and model cloud data, for the variables of mean SED and mean cloud temperature. The SED data was then compared with that from the radar composite and model rain-rate data to determine whether labelling using cloud data has produced results that are in line with that from the radar composite data. The mean CBT data was used to assess the relationship between CBT and precipitation rate in each of the models, and how that compares with that of the radar composite.

To further investigate the cloud temperature to rainfall rate relationship, the total area of rainfall ≥ 4 mm hr^{-1} was divided by the total area of cloud temperature ≤ 253 K (rain-cloud fractions), at hourly intervals for each of the models and the observation data. The resulting values for the fraction of deep cloud producing heavy rainfall were used to generate time series for each of the models, which were compared with one for the observation data. The same methodology was applied for the total area of rainfall ≥ 4 mm hr^{-1} occurring outside of cloud with CBTs ≤ 253 K, divided by the area of cloud with CBTs ≤ 253 K (rain-outside-cloud fractions).

To investigate the proportions of storm cell rainfall above a heavier rainfall threshold, and below a lower cloud threshold, fractions were generated for the total area of rainfall ≥ 6 mm hr^{-1} divided by that ≥ 4 mm hr^{-1} (rain-rain fractions) and the total area of cloud temperature ≤ 243 K divided by that ≤ 253 K (cloud-cloud fractions). As with the rain-cloud fractions, values and time series were generated for all three models and the observation data.

4.   Results

This chapter begins by displaying some of the contour charts used to give an overview of how the convection evolves in each dataset. Then, examples are shown to illustrate the reasoning behind the rainfall threshold chosen, and the effect of the parallax adjustment on the alignment of the two datasets. Following this, the results from data analysis are presented, organised by the variable investigated in each case, to create a clear picture as to how the different models handle each storm property, and how their simulations compare with the relevant observation data. Where the whole of the observation data is used, the results from radar composite data are arranged in line with those from satellite CBT data, to aid quick comparison.

4.1. An Overview of Convection Fields

4.1.1. Contour Plots of Rain Rates ≥ 4 mm hr $^{-1}$

The plots in Figure 4.1 clearly depict an increase in complexity of storm structure as grid-length reduces, particularly when moving from 1500 m to 500 m. There are also signs of increased organisation of convection, and both of these trends appear to have resulted in the simulated storms being more in line with the measurements made by the radar composite.

1500 m

500 m

200 m

Radar Composite
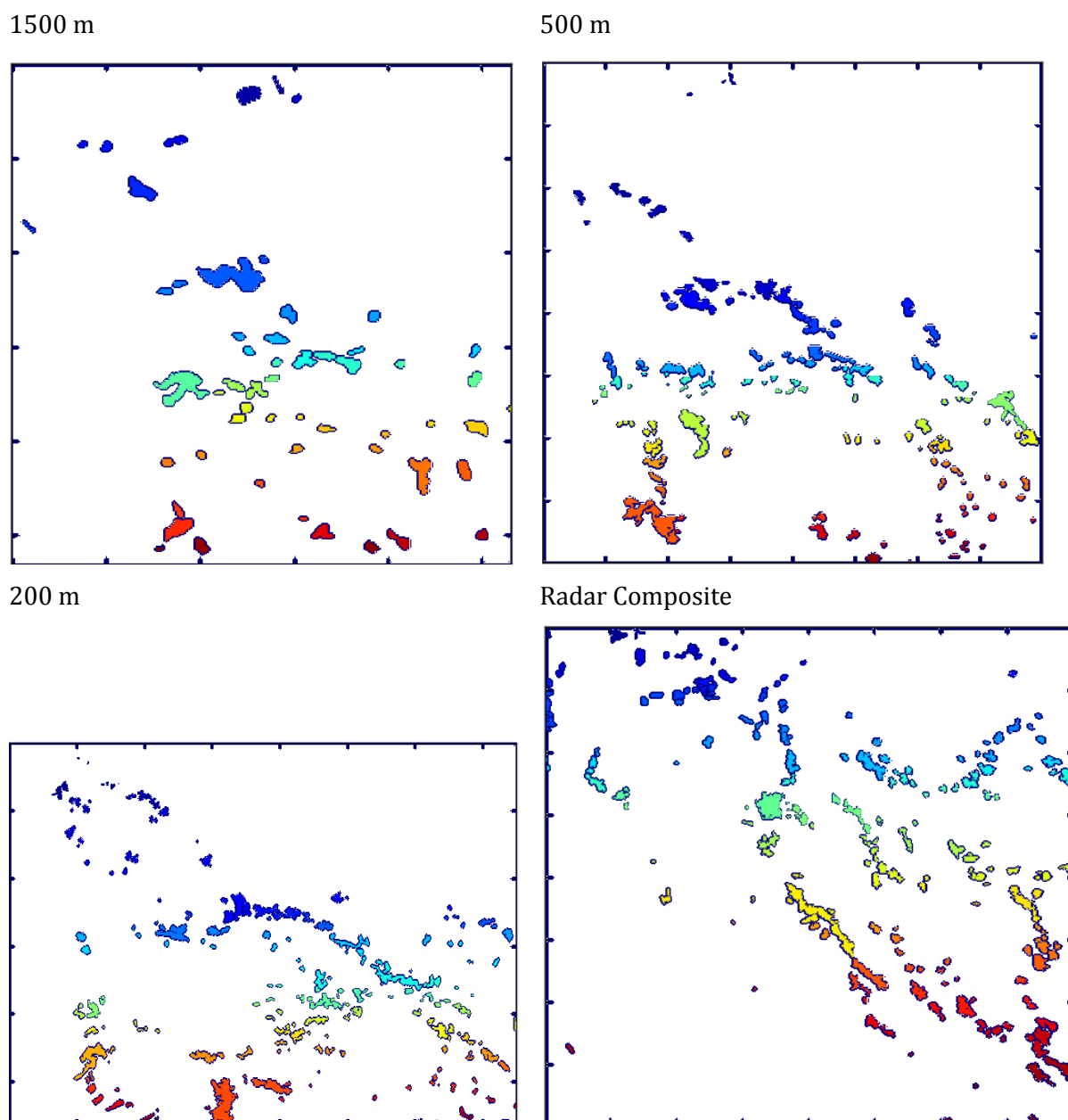
Figure 4.1: contour plots of rainfall ≥ 4 mm hr^{-1} at 14:00 for each of the datasets. Colours correspond to the label number of the storm (starting top-left). Note that the grids and domains vary between plots, so the focus is on the morphology of the deep convection.

4.1.2. Contour Plots of CBT ≤ 253 K

The cloud fields in Figure 4.2 display smaller labelled storms in each of the models, increasing in number as grid-length reduces. The 1500 m model appears to have a large deficit of cloud temperatures ≤ 253 K. By contrast, the satellite data features regions far larger than any of the models, and covering a greater proportion of the domain. This is most likely a consequence of the satellite data resolution being much lower than the model data. This also appears to have caused problems with the labelling process, which will be considered when interpreting the data analysis carried out using the labelled data from satellite fields.

1500 m   500 m

200 m   Satellite
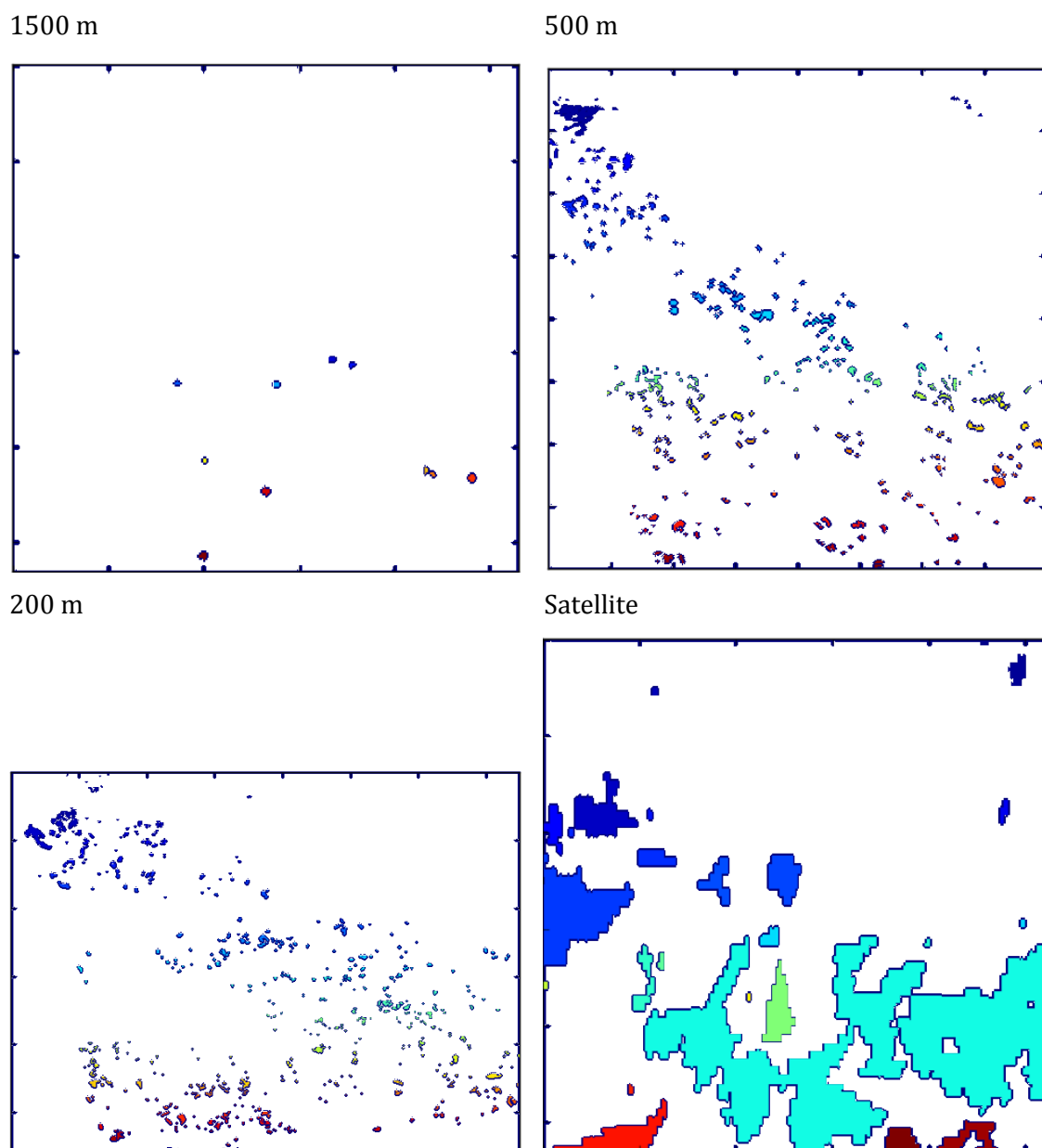
Figure 4.2: contour plots of cloud temperatures ≤ 253 K at 14:00 for each of the datasets. Colours correspond to the label number of the storm (starting top-left). Note that the grids and domains vary between plots, so the focus is on the morphology of the deep convection.

4.1.3.　　　　　Matching Radar Composite and Satellite Data

Figure 4.3A shows many areas of rain rates above the 3 mm hr^{-1} threshold value occuring outside of the deep cloud regions identified. In Figure 4.3B, it can be seen that the 4 mm hr^{-1} rain rate threshold still produced some areas outside of the deep convection, but a further increase in threshold to 5 mm hr^{-1} (Figure 4.3C) reduced the amount of identified precipitation occurring within the deep clouds further than desired, hence the 4 mm hr^{-1} threshold was chosen for the analysis process. Compared to Figures 4.3A - 4.3C, Figure 4.3D reveals a better alignment of the identified cloud with the identified rainfall, confirming the benefits of parallax correction.

(A)   (B)

C)   (D)
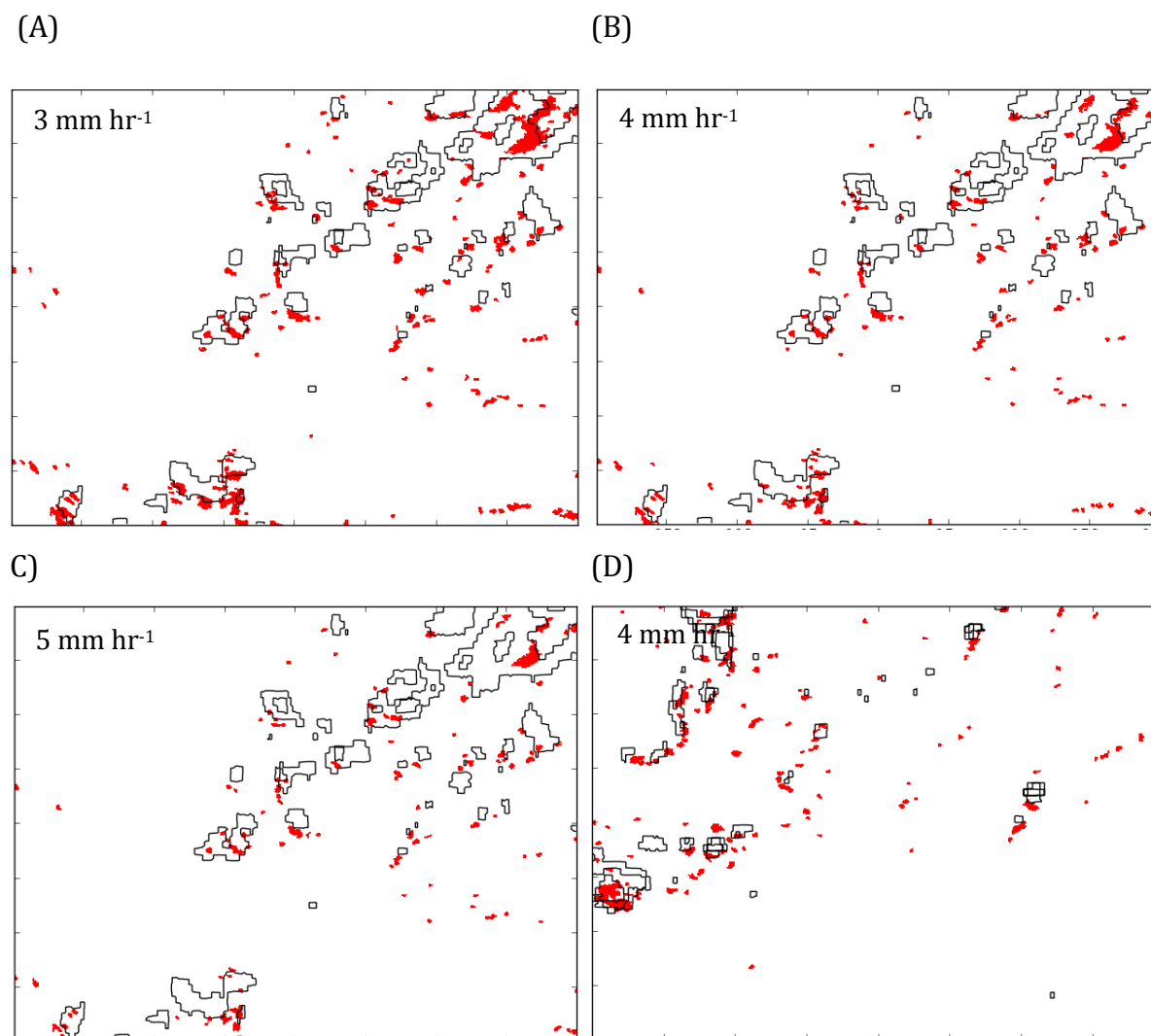
Figure 4.3: Plots of filled radar contours (red) overlaid with satellite contours (black lines). Plots A), B) and C) display the labelled rainfall for 10:15 UTC using thresholds of A) 3 mm hr^{-1}, B) 4 mm hr^{-1} and C) 5 mm hr^{-1} overlaid with contour lines of clouds $\leq$ 253 K identified from the unadjusted satellite CBT data for 10:11 UTC. Plot D) shows the identified rainfall for 10:15 UTC using the decided threshold for analysis (4 mm hr^{-1}), overlaid with contour lines of clouds at increasingly low thresholds moving from the outer lines inward (253 K, 243 K and 233 K), identified from the parallax-adjusted satellite CBT data for 10:11 UTC. Note that the adjustment required interpolation of the satellite grid to the rainfall grid, which has altered the scale of this contour plot compared to plots A), B) and C).

4.2.   Storm Equivalent Diameters (SED).

Both the rainfall (Figure 4.4A) and cloud (Figure 4.4B) data show the largest storm SED to have occurred in the 1500 m model, and the smallest in the 200 m model, with the 500 m model close to halfway between. Radar observations indicate that in terms of rain rates over 4 mm hr^{-1}, the storms in the 1500 m were too large overall, and those in the 200 m model too small, while the 500 m model produces mean SEDS that were often within 1 km of the observed values (Figure 4.4C). Satellite observations produced mean SED between around 20 km and 40 km as can be deduced from Figure 4.4D, far larger than in any of the models. This is interpreted to be a consequence of relatively low resolution data, as explained in Section 5.1.

The 1500 m model time series (Figure 4.4A) displays a lot more hour-to-hour variation than the other models and observation data, implying that cloud development and decay occurred more rapidly. Between the rain and cloud datasets, the progression of SED shows poor agreement overall for the 1500 m model, with the cloud data displaying a larger increase 1000-1100 UTC and a contrasting trend 1200-1700 UTC. The larger increase may be attributed to the 1500 m model having expanded the area of deep cloud more rapidly than the area of heavy rain, while the contrasting trends through the afternoon can be inferred to represent shallower convection decaying while deeper convection continues to develop. By the same logic, the 200 m model simulated a more gradual loss of shallower convection in favour of deeper convection, while the 500 m maintained a relatively steady ratio throughout. It is notable that for all models, the cloud data produced far lower SED than the rainfall data, indicating that heavy rain is always simulated in places where deep convection is not.

The rate of change in SED from rain data relative to that from cloud data changed across time and also differed between models. This indicates differences in the rate of deep cloud expansion relative to heavy rain expansion, which are further investigated using rain-cloud fractions in Section 4.4.

(A)
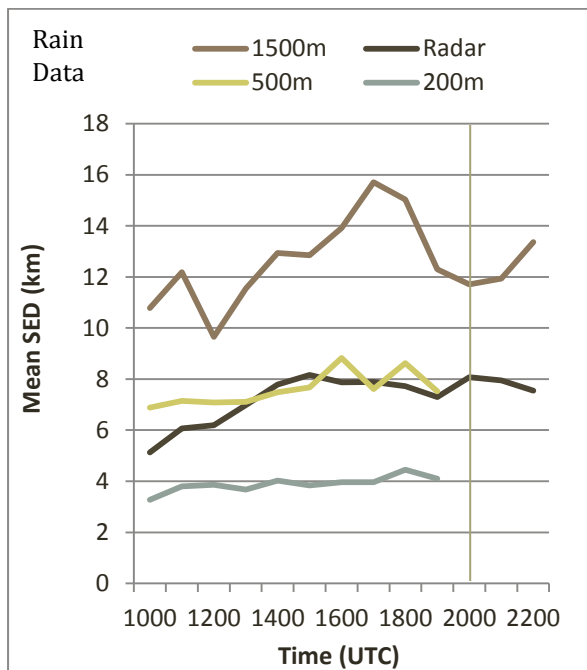
(B)
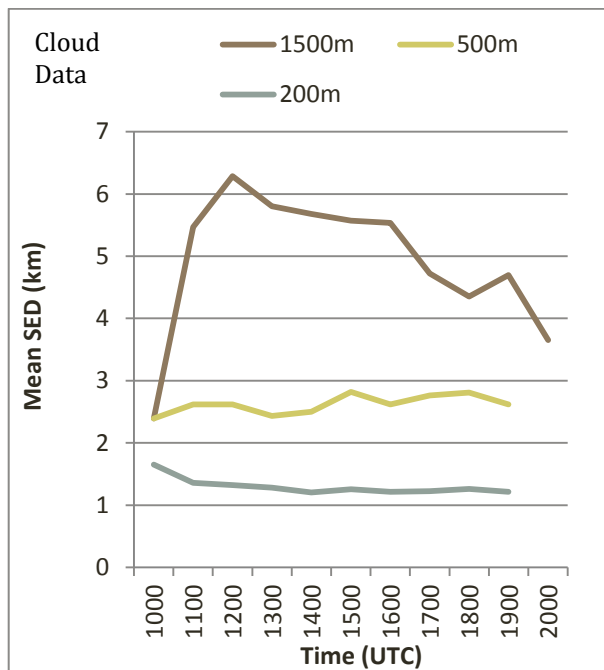
(C)
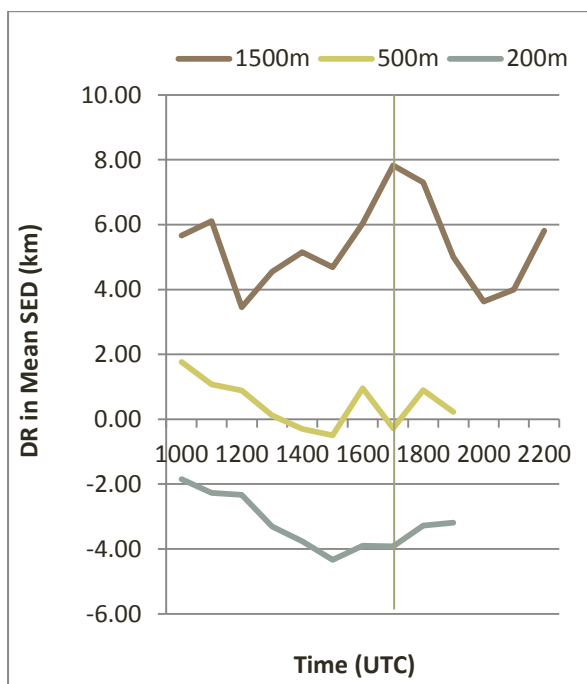
(D)
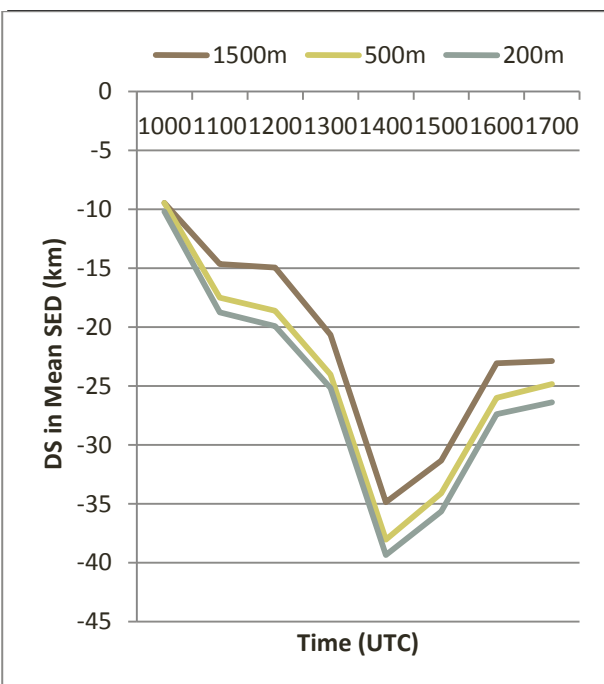
Figure 4.4: time series plots for storm equivalent diameters (SED), of (A) mean SED from rain data, (B) mean SED from cloud data (the satellite values are ommited because they were larger to the extent that they made the model behaviour difficult to see clearly), (C) differences to radar composite values (DR) calculated from the data in (A), and finally (D) differences to satellite values (DS) calculated from the data in (B).

The differences to radar proportions for normalised model cloud data (DRP) in Table 4.1A are negative for small storms and positive for large storms for both the 1500 m and 500 m models. For the medium sized storms, DRP are generally small. This implies that in terms of rain rates at or above 4 mm hr^{-1}, the proportion of large storms compared to small ones was erroneously large. It is therefore likely that the ratio of small to large storms played a large role in the differences to the radar composite data observed in the time series of mean values. The 200 m has small DRP for all size categories, despite having far too many storms overall (See Appendix A), suggesting that the model has performed well with respect to SED.

In Table 4.1B, the differences to satellite proportions (DSP) indicate that almost all of the simulated storms were smaller than those identified from satellite data, even in the case of the 1500 m model. This is inferred to be a consequence of the satellite data having a 10 km^2 resolution, as explained in Section 5.1.

Table 4.1: (A) Differences to radar proportions (DRP) for normalised rainfall data and (B) Differences to satellite proportions (DSP) for non-normalised cloud data (displayed instead of normalised data because they are more informative in this case). The SEDs are grouped into low (3-10 km), medium (10-15 km) and high (15-25 km) categories.

Rainfall Data:
DRP: STORM EQUIVALENT DIAMETER (km)

Time (UTC)	1500m Small (3-10km)	Medium (10-15km)	Large (15-25km)	500m Small (3-10km)	Medium (10-15km)	Large (15-25km)	200m Small (3-10km)	Medium (10-15km)	Large (15-25km)
1000	-28	12	17	-27	-2	29	-11	2	9
1100	-31	5	27	-32	1	32	-6	-5	10
1200	-10	1	9	-34	5	28	-9	4	5
1300	-20	7	13	-22	-2	24	4	-10	6
1400	-26	14	12	-14	-7	21	8	-11	3
1500	-20	0	20	-18	-2	21	6	-10	4
1600	-25	-1	26	-20	-12	32	8	-9	2
1700	-37	4	32	-11	-12	22	3	-8	5

More Than -60	-30 to -60	-30 to -10	-10 to +10	+10 to +30	+30 to +60	More Than +60

(A)

Cloud Data:
DSP: STORM EQUIVALENT DIAMETER (km)

Time (UTC)	1500m Small (3-10km)	Medium (10-15km)	Large (15-25km)	500m Small (3-10km)	Medium (10-15km)	Large (15-25km)	200m Small (3-10km)	Medium (10-15km)	Large (15-25km)
1000	100	0	-100	91	5	-95	100	0	-100
1100	100	0	-100	85	13	-98	100	0	-100
1200	88	13	-100	92	8	-100	100	0	-100
1300	100	-20	-80	91	-11	-80	100	-20	-80
1400	89	11	-100	88	11	-99	100	0	-100
1500	100	-100	0	82	-85	3	100	-100	0
1600	100	0	-100	82	18	-100	100	0	-100
1700	100	0	-100	86	11	-97	100	0	-100

More Than -60	-30 to -60	-30 to -10	-10 to +10	+10 to +30	+30 to +60	More Than +60

(B)

4.3.   Storm Average Rain Rates and Cloud Brightness Temperatures (CBT).

The progression of rain rates (Figure 4.5A) in all three models follows that of the radar composite in terms of the overall shape, though the 1500 m model peaks around an hour too late while the 500 m and 200 m models both peak around an hour too early. In terms of CBT (Figure 4.5B), when taking colder cloud tops to be associated with higher rainfall rates, the cloud data for the observations and the 1500 m model match well with the rainfall data. For the 500 m and 200 m models, however, the progression of CBT does not display much similarity with the progression of rain rates, and Figure 4.5B depicts a warming of mean CBTS 1000-1200 UTC, when Figure 4.5A shows a contradictory drop overall in the satellite observation data. The respective trends then reverse 1300-1700 UTC, and again this is not what was expected from the 500 m and 200 m models, as rain rates are seen to be reducing during that time.

The most intense rain rates were simulated by the 500 m model, and these are associated with the largest differences to radar observations (DR) 1000-1400 UTC shown by Figure 4.5C, as the radar composite lies at the low end of the range during this time, with the 1500 m and 200 m models being relatively close to it. The lowest DR overall were achieved by the 200 m model, which performs particularly well 1600-1900 UTC. While the 1500 m model values are also relatively close to the observation data for the differences to satellite observations (DS) visible in Figure 4.5D, the 200 m model has the largest DS 1000-1500 UTC, contrasting with what is seen in the rainfall data. The very similar behaviour of the 500 m model is again evident.
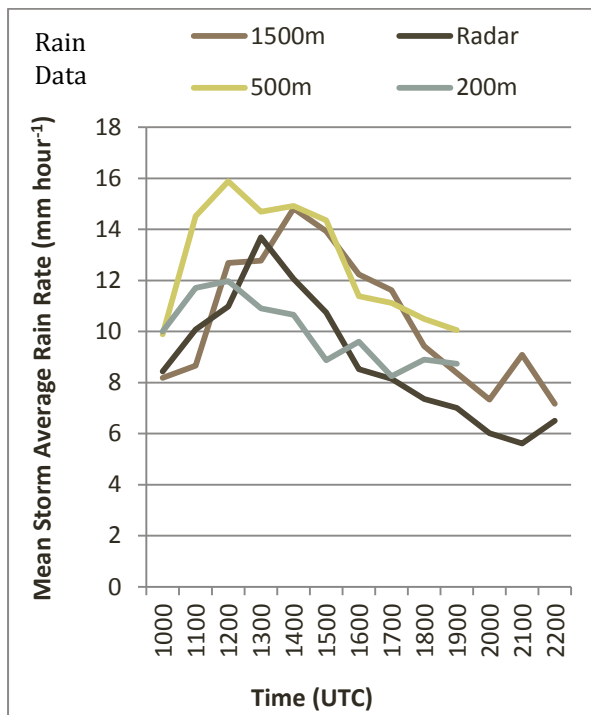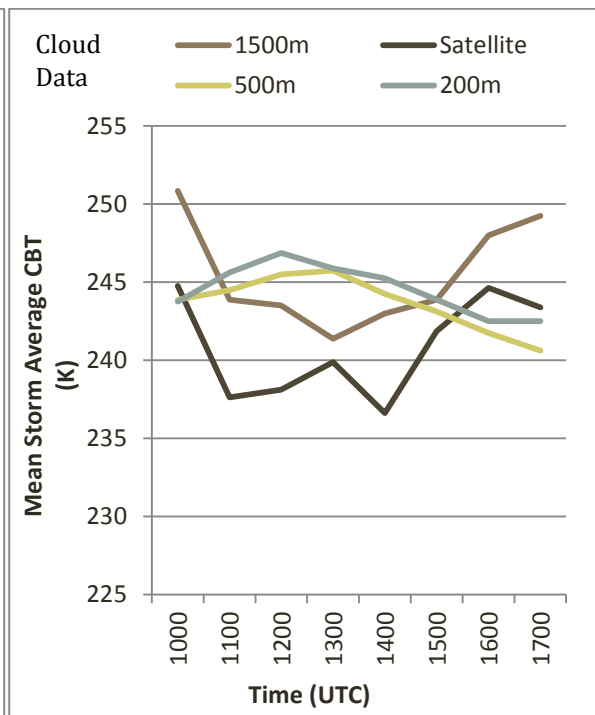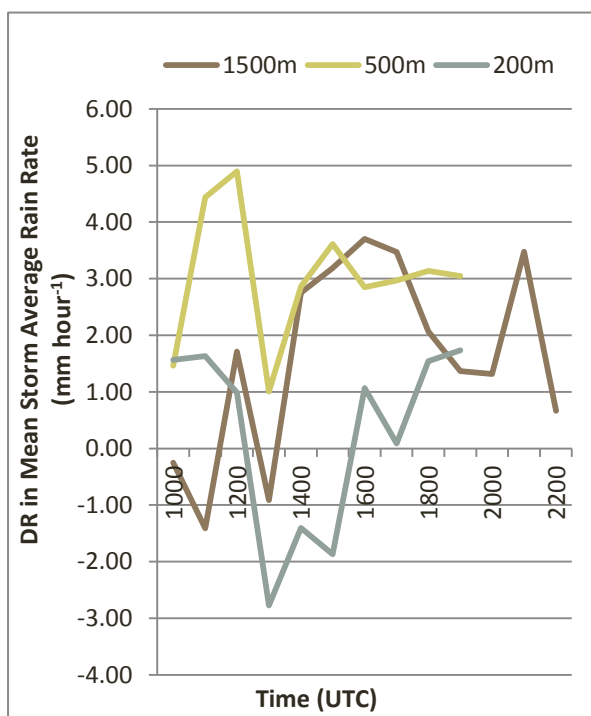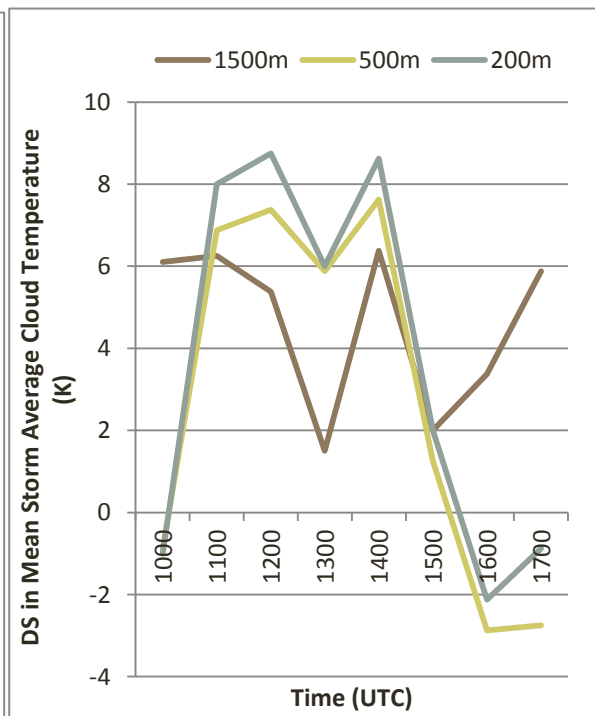
Figure 4.5: time series plots using rain rate and CBT data, for A) mean storm average rain rate (mm hr $^{-1}$), B) mean storm average CBT (K), C) difference to radar observations (DR) in mean storm average rain rate (mm hr $^{-1}$), and D) difference to satellite observations (DS) in mean storm average CBT (K).

The DSP for cloud depths based on CBTs (Table 4.2B) show no clear trend with reducing grid-length, not just in terms of overall distribution, but also the evolution through time. This is not the case when observing the differences to satellite frequencies (DSF) for CBTs; the DSF shown for shallow storms simulated by the 500 m and 200 m models are much higher than for deep storms, whereas there is little such difference between categories in the DSF for the 1500 m model.

Considering higher rain rates to be generally associated with lower cloud temperatures, the DRP for the 1500 m model (Table 4.2A) tie in with the DSP for the cloud data 1000-1200 UTC (Table 4.2B), but this is not so much the case 1300-1700 UTC; the DSP of deep clouds are seen to become too small overall, yet the DRP of heavy rain rates become too large. For the shallow clouds and light rain rates, the relationship is seen to remain close to that observed 1000-1200 UTC. This suggests that from noon, the 1500 m model produced heavy rain at higher cloud temperatures than is apparent in the observation data.

For both the 500 m and 200 m models, the DRP of light rain rates displayed in Table 4.2A are too high throughout, particularly in the latter case. The CBT show corresponding positive DSP for shallow clouds 1100-1400 UTC for both models, but at other times the DSP are negative, with positive DSP (Table 4.2B) instead seen for deep clouds. 1000-1600 UTC, the negative DRP of heavy rain rates in the 200 m model are reflected to some extent by negative DSP of deep clouds, as are positive light rain rate DRP by positive shallow cloud DSP. The light rain to shallow cloud relationship depicted is very similar for the 500 m model. For storms with heavy rain rates, DRP for this model are shown to be small, while there is a mix of positive and negative EP of storms with low CBT, giving no clear relationship.

These results give the impression that increasing the resolution from 1500 m to 500 m or 200 m has only served to produce an excess of shallow storms during the middle part of the day (1000-1400 UTC), followed by numbers of storms closer to that observed but with CBTs that are in the order of 2-4K too low. As the ratio of these to midrange and deep (243-223 K) storms reduced 1400-1700 UTC, particularly in the 500 m model, it is inferred that the relatively shallow storms in the simulations were dissipating during this time, while the deeper storms persisted. This explains the reducing mean CBTs 1000-1200 UTC in the 500 m and 200 m models followed by a steady fall 1200-1700 UTC. Curiously, the rain rate to CBT relationship in the 500 m and 200 m models is interpreted to have been close to that of the observation data during the period in which there was an excess of shallow storms, while at other times, the amount of heavy rain was too low for the CBTs simulated. This behaviour is visible in the non-normalised data (Tables 4.3A and 4.3B) as well as the normalised data (Tables 4.2A and 4.2B).

Table 4.2: A) DRP for normalised model rainfall data and B) DSP for normalised model cloud data, both in percent. The frequencies are grouped into light (4-6 mm hr $^{-1}$), moderate (6-12 mm hr $^{-1}$) and heavy (12-30 mm hr $^{-1}$) categories of storm average rain rate for A) and deep (CBT 223-233 K), midrange (CBT 233-243 K) and shallow (CBT 243-253 K) categories of cloud depth for B). Note that these depth terms are relative; all CBTs at or below 253 K are considered to represent deep convection.

Rainfall Data:
DRP: STORM AVERAGE RAIN RATE (mm hr $^{-1}$)

1500m Time (UTC)	Light (4-6 mm hr⁻¹)	Moderate (6-12 mm hr⁻¹)	Heavy (12-30 mm hr⁻¹)	500m Time (UTC)	Light (4-6 mm hr⁻¹)	Moderate (6-12 mm hr⁻¹)	Heavy (12-30 mm hr⁻¹)	200m Time (UTC)	Light (4-6 mm hr⁻¹)	Moderate (6-12 mm hr⁻¹)	Heavy (12-30 mm hr⁻¹)
1000	19	7	-26	1000	46	-37	-9	1000	56	-27	-28
1100	33	12	-45	1100	25	-16	-9	1100	49	-13	-37
1200	21	-14	-6	1200	22	-30	8	1200	42	-9	-33
1300	0	18	-18	1300	21	-6	-14	1300	43	4	-47
1400	-3	-1	4	1400	20	-14	-5	1400	42	-2	-40
1500	3	-16	13	1500	25	-25	0	1500	49	-15	-35
1600	-6	-14	20	1600	17	-21	4	1600	32	-9	-22
1700	-12	-7	19	1700	27	-26	-1	1700	52	-22	-30

More Than -60	-30 to -60	-30 to -10	-10 to +10	+10 to +30	+30 to +60	More Than +60

A)

Cloud Data:
DSP: STORM AVERAGE CBT (K)

1500m Time (UTC)	Deep (223-233K)	Midrange (233-243K)	Shallow (243-253K)	500m Time (UTC)	Deep (223-233K)	Midrange (233-243K)	Shallow (243-253K)	200m Time (UTC)	Deep (223-233K)	Midrange (233-243K)	Shallow (243-253K)
1000	-10	-40	50	1000	9	-5	-4	1000	-3	14	-11
1100	-37	15	22	1100	-35	5	31	1100	-43	5	38
1200	-29	25	13	1200	-27	6	30	1200	-32	4	36
1300	0	33	-17	1300	-14	15	14	1300	-16	19	13
1400	10	-2	21	1400	15	-14	29	1400	7	-10	33
1500	-10	25	-8	1500	1	8	-2	1500	-7	15	-1
1600	-11	-9	24	1600	12	16	-22	1600	1	27	-23
1700	-14	-19	42	1700	21	10	-22	1700	2	25	-18

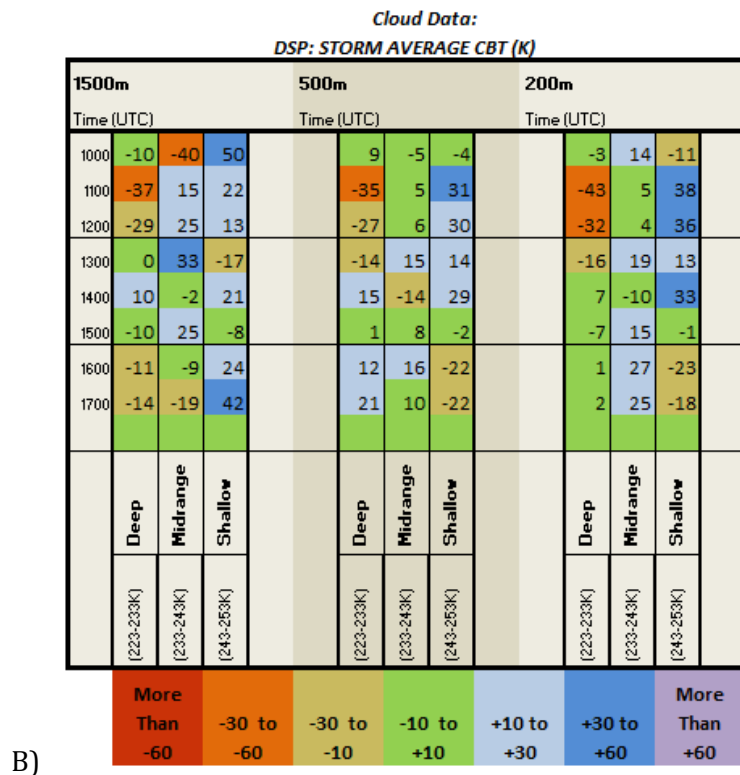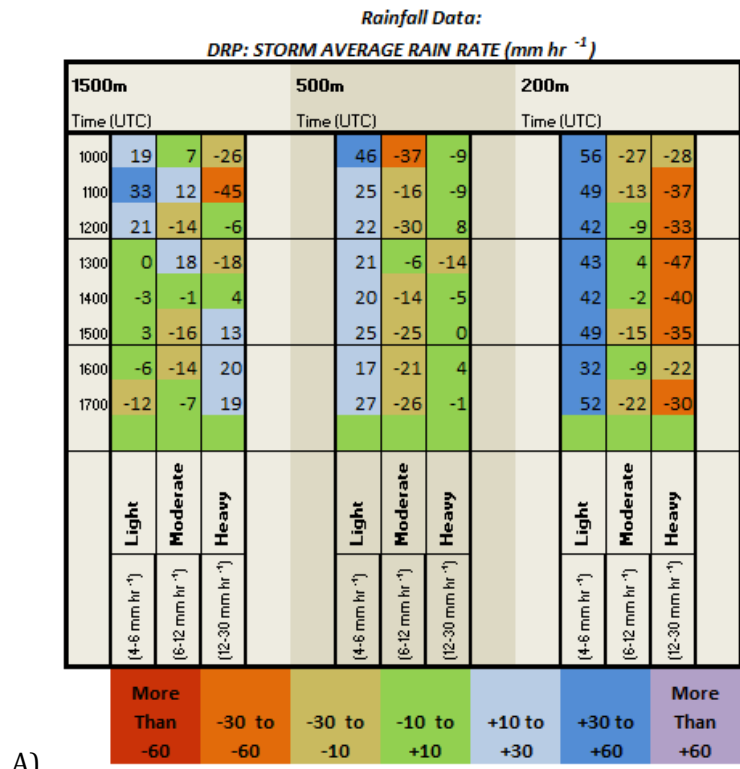| More Than -60	-30 to -60	-30 to -10	-10 to +10	+10 to +30	+30 to +60	More Than +60

B)

Table 4.3: A) differences to radar frequencies (DRF) for model rainfall data, for rain rates grouped into categories as in Table 4.2A, and B) differences to satellite frequencies (DSF) for model cloud data, for clouds grouped into categories as in Table 4.2B.

Rainfall Data:
DRF: STORM AVERAGE RAIN RATE (mm hr⁻¹)

1500m Time (UTC)	Light (4-6 mm hr⁻¹)	Moderate (6-12 mm hr⁻¹)	Heavy (12-30 mm hr⁻¹)		500m Time (UTC)	Light (4-6 mm hr⁻¹)	Moderate (6-12 mm hr⁻¹)	Heavy (12-30 mm hr⁻¹)		200m Time (UTC)	Light (4-6 mm hr⁻¹)	Moderate (6-12 mm hr⁻¹)	Heavy (12-30 mm hr⁻¹)
1000	2	-26	-29		1000	18	-37	-19		1000	92	-4	-15
1100	0	-29	-66		1100	23	-21	-20		1100	86	-4	-30
1200	7	-53	-59		1200	27	-49	-4		1200	101	15	-32
1300	-4	-10	-59		1300	32	-4	-9		1300	127	53	-34
1400	-16	-46	-69		1400	21	-36	-33		1400	92	5	-69
1500	-14	-50	-39		1500	25	-44	-15		1500	80	-22	-54
1600	-31	-51	-24		1600	0	-45	-15		1600	18	-31	-39
1700	-28	-50	-27		1700	14	-47	-17		1700	27	-47	-45

Legend: More Than -60 | -30 to -60 | -30 to -10 | -10 to +10 | +10 to +30 | +30 to +60 | More Than +60

A)

Cloud Data:
DSF: STORM AVERAGE CLOUD TEMPERATURE (K)

1500m Time (UTC)	Deep (223-233K)	Midrange (233-243K)	Shallow (243-253K)		500m Time (UTC)	Deep (223-233K)	Midrange (233-243K)	Shallow (243-253K)		200m Time (UTC)	Deep (223-233K)	Midrange (233-243K)	Shallow (243-253K)
1000	-2	-8	-9		1000	8	10	14		1000	2	23	12
1100	-7	-1	1		1100	5	38	50		1100	0	71	105
1200	-7	3	1		1200	5	54	87		1200	2	115	213
1300	1	9	-2		1300	14	84	127		1300	21	183	252
1400	3	9	10		1400	51	113	161		1400	36	211	286
1500	-1	9	2		1500	59	167	158		1500	37	270	217
1600	-2	-3	0		1600	105	221	137		1600	53	278	135
1700	-3	-5	0		1700	136	141	101		1700	56	195	114

Legend: -30 to -10 | -10 to +10 | +10 to +30 | +30 to +60 | +60 to +100 | +100 to +200 | More Than +200

B)

4.4.   Fraction Statistics

It is clear from Figure 4.6A that the 1500 m model had persistently higher fractions of cloud producing rain than the other models and observation data, and by a substantial amount, indicating that rain rates ≥ 4 mm hr $^{-1}$ were being simulated from far more of the deep cloud (CBT ≤ 253 K). Relative to this model, the other two were close to the observation data, but the trend seen 1000-1300 UTC is in the opposite direction, resulting in fractions too large, before a recovery 1400-1700 UTC.

Despite the improvement with resolution, results in Figure 4.6B show the majority of simulated rain rates ≥ 4 mm hr $^{-1}$ be occurring outside of deep convection at all times studied, whereas in the observation data, the majority is seen to be within deep convection, particularly 1300-1700 UTC. This gives the impression that the simulations were producing heavier rain from temperatures > 253K than should have been the case.

As resolution increases, Figure 4.6C shows a reduction in the area of rain rates ≥ 6 mm hr $^{-1}$ relative to that with rain rates ≥ 4 mm hr $^{-1}$ (the rain-rain fraction). This also brings the simulated values ever-closer to those from observation data, with the 200 m model displaying a close match to observations. This implies that the rain rates tended to be too high in the 1500 m and 500 m models, with only the 200 m model managing to accurately represent them. Despite these differences, the progression of rain rates through time for each of the datasets has been found to follow roughly the same shape. This suggests that the rate at which precipitation intensified within storms up to rates of over 6 mm hr^{-1} was well handled by all of the models, with little benefit from increasing the resolution.

Compared to observations, the area of cloud at or under 243 K divided by that under 253 K (cloud-cloud fraction, illustrated by Figure 4.6D) is always lower in the 1500 m model, but the progression through the day has the right shape overall. It is inferred that while the rate at which cloud deepens was well handled, the depth was being persistently underdone. The 500 m and 200 m models display very different behaviour; cloud-cloud fractions begin too high at 1000 UTC, become too low 1200-1300 UTC, then increase markedly to finish far too large 1600-1700 UTC. Not only this, but the 1000-1100 UTC and 1400-1700 UTC trends with time are the reverse of those seen in the observation data. It is as if clouds became too deep on average by 1000 UTC, only for shallow storms to have then become dominant 1100-1400 UTC, contrary to the situation interpreted from the observation data. After this time, they quickly subsided in favour of storms which were once again too deep on average, particularly 1600-1700 UTC.

(A) Rain-Cloud Fraction
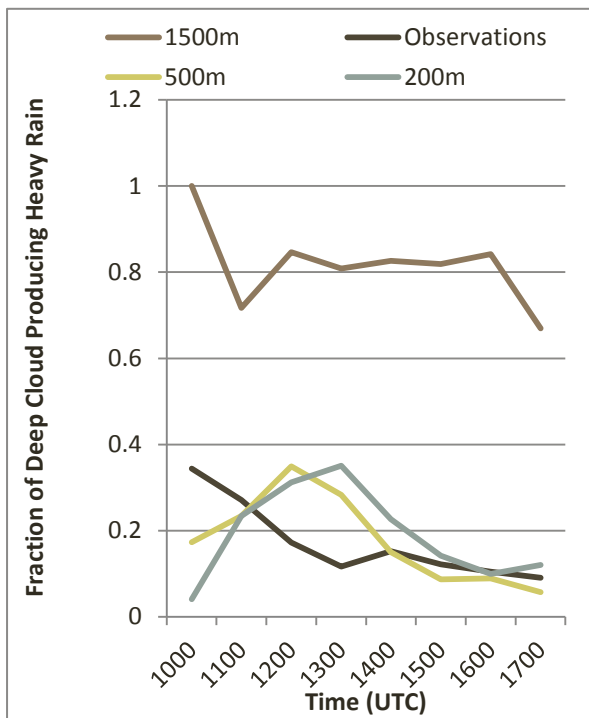
(B) Rain-Outside-Cloud Fraction
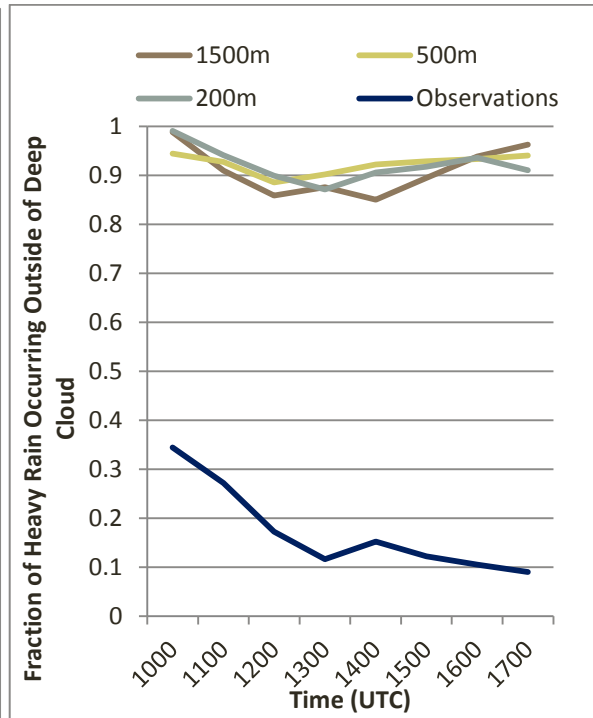
(C) Rain-Rain Fraction
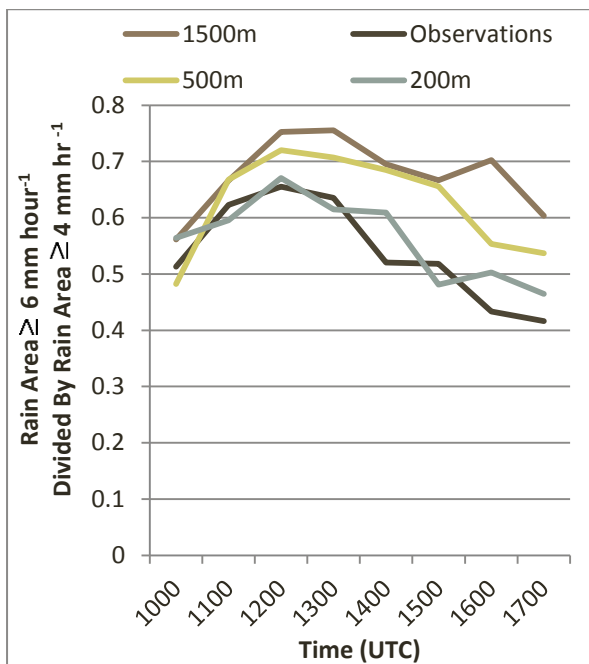
(D) Cloud-Cloud Fraction
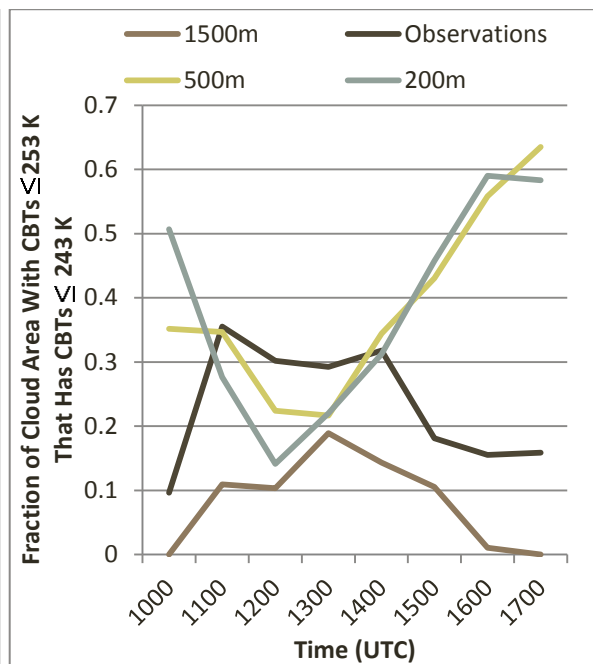
Figure 4.6: time series plots of fractions obtained by dividing A) area of CBT $\leq$ 253 K with rain rates $\geq$ 4 mm hr^{-1} by the total area of CBT $\leq$ 253 K, B) area of CBT $\geq$ 253 K with rain rates $\geq$ 4 mm hr^{-1} by the total area of rain rates $\geq$ 4 mm hr^{-1}, C) area with rain rates $\geq$ 6 mm hr^{-1} by the area with rain rates $\geq$ 4 mm hr^{-1}, and D) area of CBT $\leq$ 243 K by the area of CBT $\leq$ 253 K.

4.5.   'Blob Factor' Analysis

The mean centroid-max rain rate differences in location as proportions of the mean SED (CMD/SED) are depicted in Figure 4.7 to have become larger as model resolution increased, giving cause to accept the hypothesis that storms become less like blobs as grid-length reduces. This in turn reduced the overall difference to the CMD/SED of the radar composite data, particularly when grid-length was reduced from 1500 m to 500 m. Clearly there was a tendency for storms in the 1500 m to be closer to rounded features with rain rates increasing towards the centre (in effect, more like blobs) than the observation data suggested to be true of reality. However, this did not manifest at all times, and the variation through time seen in Figure 4.7 is relatively large, with the differences to radar composite values substantially larger during the middle part of the day (1100-1530 UTC) and the final two hours (2000-2200).

Considering the behaviour through time, differences between the models may reflect the storms having developed at different times more than their handling of rain rate distributions within those storms. Even so, observing the general trends across numbers of hours, a few observations can be made. The radar composite data values in Figure 4.7 show no overall change in CMD/SED 1000-1630 UTC, whereas an increase is seen in the 500 m and 200 m values. The 1500 m model CMD/SED are too variable across this period to reliably determine if a trend exists or not. During the final two hours, the radar composite data is seen to produce higher CMD/SED compared to the preceding couple of hours, which the 1500 m model fails to capture.
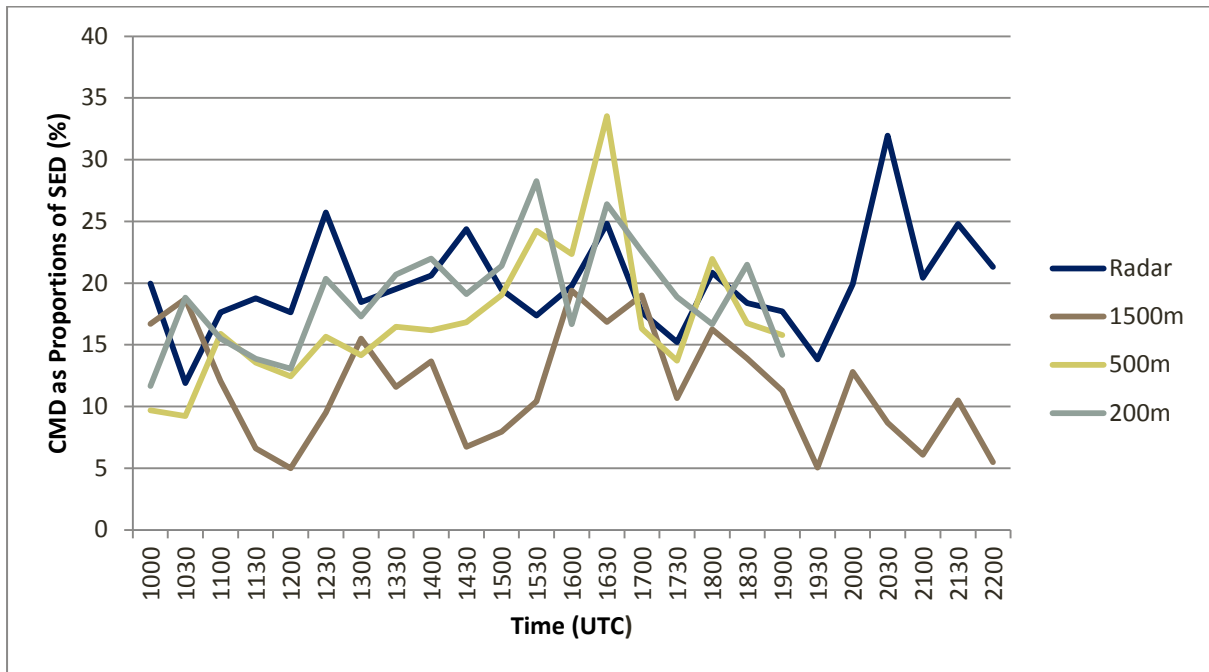
Figure 4.7: time series plots of the mean centroid to max rain rate differences in location (CMD), as a proportion of the mean SED (CMD/SED), for labelled storms.

An examination of how CMD/SED relates to mean SED (Figure 4.8), conducted in response to the variability through time displayed by the 1500 m model, has revealed spreads for which only very weak correlations can be determined for three of the four datasets (illustrated by poor linear fits as an example). The exception is the 500 m model, although the correlation remained unimpressive (R^2 value of 0.52). The changes in mean SED with resolution are clearly apparent and in line with the results for this variable examined earlier.

Seeking instead a relationship between CMD/SED and the storm average maximum rain rates (Figure 4.9) has found stronger positive correlations for the radar composite and 1500 m model, but R^2 values (again, linear values shown as examples) remained rather low considering the limited size of the datasets. The maximum rain rates appear to have been far too high in the 1500 m model compared to those of the radar composite, and a little too low in the 200 m model, with the 500 m model displaying good accuracy.
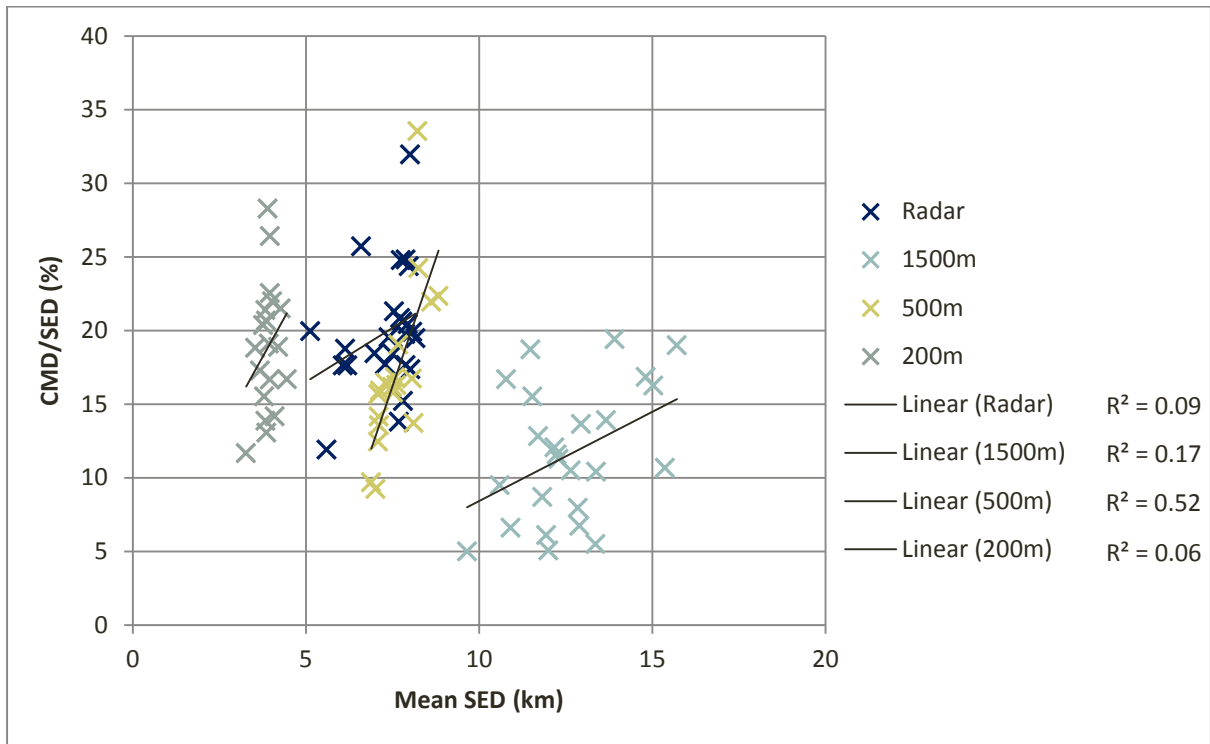
Figure 4.8: scatter plot of CMD/SED (%) against associated mean SED (km), with R-square values shown as part of the legend.
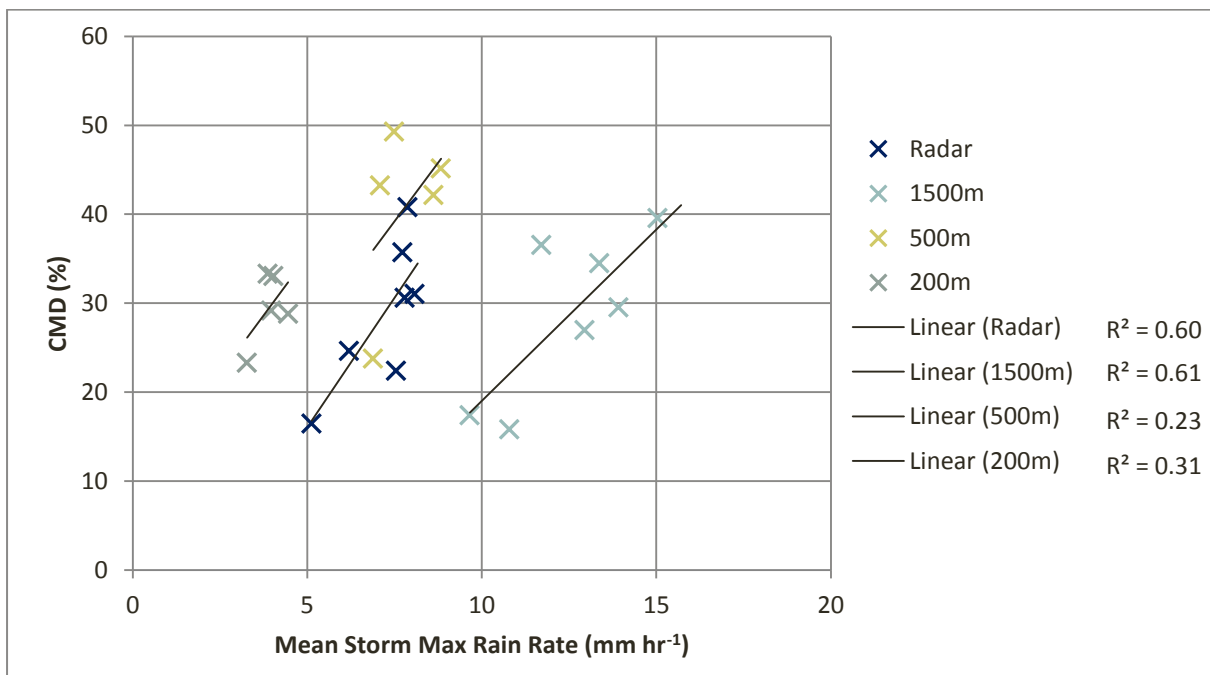
Figure 4.9: scatter plot of CMD/SED (%) against associated mean storm max rain rates (mm hr^{-1}), with R-square values shown as part of the legend.

5.   Discussion

In this chapter, the first section describes a significant problem encountered when using satellite data to assess the model performance. In the second section, results for each storm property are discussed in light of the existing literature on high resolution model characteristics and performance covered in chapter 1. The effectiveness of the analysis methods are assessed, along with the applicability of the satellite data used.

5.1.   The Resolution Problem

All of the results that have used satellite CBTs must be discussed with respect to a problem that occurred due to a large difference in resolution between the satellite data and the other datasets used. The labelling process used could not identify any storms below 10 km size in the satellite data, due to the near-10 km resolution. This was not true for the model and radar composite datasets, and so the numbers and proportions of storms below 10 km in size appeared much lower when using the satellite data, regardless of whether this was truly the case. Among the models, the 1500 m model had relatively low identified storm counts (apparent when comparing contour plots for the different models in Sections 4.1.1 and 4.1.2), which means the impact that this had on the time series of mean and fraction values for this model was considerably less than for the 500 m and 200 m models. In these cases, the labelling process identified large numbers of small, shallow storms, which appeared to be large surpluses when compared to the satellite data. This is considered to be a misleading result given the effect of the much lower satellite resolution, and the discussion of results in Section 5.2 takes this into consideration, referring to this issue as the resolution problem.

5.2.   Discussion of Results

The comparison of mean values generated from storm rainfall fields in the models with those in the radar composite data has, as expected, produced similar results to those of Hanley *et al*. (2014), in which the same data is used. Significant examples are the matching relative position of the models in terms of SED and rain rate means, the timing of peak mean rainfall in the models relative to each other and the radar composite, and the better handling of storm mean rain rates by the 200 m model compared to the others. The presence of overly broad storms in the 1.5 km model, reducing as resolution increases, was also observed by Stein *et al*. (2014) for shallow cases, implying that the relationship is similar for both deep and shallow storms. Combining observations, it appears that the main difference occurs for the 200 m model, in the simulated sizes of shallow storms are close to correct, as opposed to undersized for deep

storms. As for the time of storm initiation, errors in the 1.5 km model are also observed by Morcrette *et al.* (2007), while the tendency for convection to initiate earlier also manifested in results from idealised studies conducted by Petch (2006), who attribute this behaviour to increasingly focused diffusion, eroding capping inversions faster at favourable points. Some differences to the results obtained by Hanley *et al.* (2014) have been observed too, but these can be attributed in large part to the use of much lower minimum area thresholds when labelling storms in this case; for example the 500 m model was analysed using a threshold of 0.25 km^2 as opposed to 10 km^2 in the case of Hanley *et al.* (2014). Given that the same thresholds have been applied to the satellite CBT data, these differences are not considered to be problematic for comparison of the two datasets.

For the 1500 m model, the results from comparison of model and observation mean values for rain rates with those for CBTs were generally in line with what was expected from the literature reviewed. By contrast, the results from same form of analysis applied to mean values for the 500 m and 200 m models, and distributions for all of the models, were unexpected. This is considered most likely to be a consequence of the resolution problem, being largely responsible for the apparent excess of small, shallow clouds at most times in the 1500 m model and throughout 1000-1500 UTC in the 500 m and 200 m models, as opposed to model error.

Results from analysis of SED distributions using rain data were in good support of the observations in Hanley *et al.* (2014) and Lean *et al.* (2008), illustrating the tendency of the 1500 m and 500 m models to produce oversized storms, though the results in this study appeared to show this happening to a greater extent. In terms of frequencies, the much greater lack of small storms observed in the 1500 m model (also clearly apparent in the differences in frequency to radar composite data in Appendix A) ties in with the comparison of the two models in Hanley *et al.* (2014). This is also true of the accurate representation of storm size distribution seen in the 200 m model, at least for SED of 8 km and above. This was achieved despite having far too many storms overall, and displays both the improved representation of storm development beyond initiation that is expected with increased resolution (e.g. Done *et al*, 2004) and a tendency to produce excessive cases of deep convection, attributed by Lean *et al.* (2008) to CAPE building up during the spin-up period, before a sudden release once convection becomes sufficient.

The distributions of SED from rain data analysis have been strongly supported by results using cloud data, despite the resolution problem. Considering this, the undersized mean SEDs derived from cloud data, combined with rain-cloud ratios larger than observed, implies that the dynamical representation in the models did not develop deep cloud rapidly enough relative to

heavy rain. The improvement with increasing model resolution, also observed with regard the size of intense precipitation cores relative to the storms, likely reflects the benefits of an increasing proportion of the microphysical processes being solved (Done *et al*, 2004). Unfortunately, the resolution problem substantially reduces the confidence in these results.

The distributions of rain rates for the 1500 m model are for the most part in agreement with previous studies of models with such resolution, and the observed behaviour of the UKV (e.g. McBeath *et al.*, 2014). For example, Lean *et al.* (2008) found excessive numbers of storms with light rain rates in studies of a 1000 m model, while a 4000 m model had a deficit for rates of 1-2 mm hr^{-1}, so allowing for variations between case studies, the lack of light rain rates that this study has observed in the 1500 m model seems a realistic observation.

The DSP for cloud-derived CBTs were largely uninformative, with no sign of a reduction in the proportion of large clouds relative to observations as grid length was reduced from 1500 m to 500 m, which was anticipated in light of the cloud broadness results in Stein *et al.* (2014). The fact that the area of cloud with CBTs $\leq$ 253 K associated with each storm was found to be on average smaller than the area of rain rates $\geq$ 4 mm hr^{-1} in all of the simulations, particularly that of the 1500 m model, explains a lot of the disagreement observed. The expected trend in large clouds was, however, observed in the actual frequencies for the models, implying that the resolution problem also played a role in making comparison with satellite data ineffective.

Aside from some degree of logical relationship between the rain rates and CBTs for the 1500 m model, there was little in the way of expected behaviour of one variable with respect to the other. An anticipated negative correlation between cloud top temperatures and heavy precipitation within deep convection was not discernable in the 500 m and 200 m model data covering a large part of the day being studied. A likely explanation for much of the discrepancy with expectations again comes from the resolution problem, as it only had an impact on the cloud data analysis, and not that of the rain data. While this also makes any assessment of model accuracy unreliable, the dissipation of a large proportion of the shallower clouds in the 500 m and 200 m models (inferred in Section 4.2.) 1500-1700 UTC reduced the effect of the resolution problem to some extent, so it could be interpreted that the excessively deep clouds depicted by the 1500-1700 UTC data for these two are more a reflection of model inaccuracies. The significance of this observation is low as a result of only 29 storms being identified within the 10-25 km range by SEVIRI, but evidence of errors arising from under-resolved convection in the results of Bryan and Rotunno (2005) and Petch (2006) give some support.

The deduction from rain-cloud fraction results, that heavy rain is simulated to be occurring from too much of the deep cloud by the 1500 m model, is along the lines of that made by

Stein *et al.* (2014) regarding the convective cores of deep storms. Increasing the model resolution better represented the cores, and hence the overall rain-cloud fractions became more accurate. This also explains the rain-rain fraction results; larger cores are likely to feature larger areas of rain rates ≥ 6 mm hr^{-1}, and so as core representation improved, the rain-rain fractions become more accurate as well. Combining these deductions with the rain-cloud fraction results for the 500 m and 200 m models, it is apparent that they were developing cores too rapidly relative to the expansion in deep cloud area of the associated storms. However, it is considered likely that the resolution problem detailed earlier has produced lower rain-cloud fractions for the observation data than would have been calculated had the radar composite resolution matched that of the satellite data (rain areas would have then tended to be larger relative to cloud areas). It is therefore concluded that the model simulations are probably more accurate than appeared to be the case in the rain-cloud results, with their performance better represented by the rain-rain fractions. These showed good accuracy for the 200 m model, and this again indicates improvements with resolution, although the observed gain was small relative to what has been observed for other variables. The issue regarding differences in resolution also has the implication that the amounts of heavy rain occurring within cloud areas calculated using the observation data were probably too high. While this means that the observation fractions should have been closer to the model fractions, the extent to which they differed is of such large magnitude that it seems reasonable to conclude that the models were simulating too much in the way of rain rates ≥ 4 mm hr^{-1} from clouds with CBTs warmer than 253 K. Further research is needed, using a more effective combination of rainfall and cloud observations, to determine the reliability of this deduction.

In light of the resolution problem, the cloud-cloud fraction results hold little merit in terms of assessing model accuracy; the presence such storms in the models will almost certainly have had a greater lowering effect on the total area of cloud ≤ 243 K compared to that ≤ 253 K than seen in the satellite data. The progression of cloud fractions in the 500 m and 200 m models illustrated this process clearly, when considering how the frequencies of small storms developed through the day (outlined when discussing the results from the distribution data). While this means the apparent accuracy results were probably misleading, the difference to the 1500 m model observed is considered realistic; with the majority of simulated storms in the 1500 m having been large, and a greater proportion of them deep compared to the 500 m and 200 m models, it is logical to expect higher fractional coverage of the deep cloud regions by cloud with temperatures ≤ 243 K.

The agreement of the 'Blob Factor' results with the hypothesised relationship between model resolution and the distance of maximum rain rates from the approximate storm centres

suggests that CMD could be an effective means of measuring the typical shape of observed and simulated storms. The periods when storms were too blob-like in the 1500 m model may have been those with larger SED and higher mean storm maximum rain rates, but the relationships found were too weak to draw significant conclusions without a larger dataset. Such could be obtained by calculating values at a higher temporal resolution, or through the combination of data from more than one case study. The change in the strength of the correlations between these variables displayed no clear relationship with changes in data resolution, and this could mean one of two things; that changing resolution had no significant effect on the relationships, or that the relationships were not significant in the first place. Again, further investigation is required to establish whether the 'Blob Factor' is dependent on variables other than the grid-length of the model.

Having encountered the resolution problem as outlined in Section 5.1, a possible workaround, whereby analysis of the labelled model data is restricted to storms of 10 km^2 or greater, was considered. Investigation into how many storms of 10 km^2 area and above were being modelled found that such a process would ignore a large proportion of the storms simulated by the higher resolution models (for example, more than half of them in the 500 m model, as illustrated in Appendix B). This would remove the high-resolution features that are the focus of this study, particularly the cells just after initiation that occur as a result of small, localised variations in atmospheric conditions as observed by Crook (1996). Similarly, an averaging of the model data to a 10 km^2 resolution would also remove these features, defeating the object of this project; these small details are of particular importance for small-scale developments such as convective initiation (Merk and Zinner, 2013). In light of this, and given time constraints, these two procedures were not carried out as part of this study.

The problems and limitations encountered in this study demonstrate that, to effectively combine satellite and radar composite data and conduct a truly representative analysis of how high resolution models handle cloud microphysics based on CBTs, higher resolution satellite data is required.

6.   Conclusion

This final chapter considers the extent to which the aims of the study have been satisfied, and from the results obtained, possible routes for further research are then suggested.

The results obtained from statistical analysis using satellite CBTs and model cloud top temperature data supported those obtained using radar composite and model rain rate data to some extent, but this was for the most part limited to the results from analysing the mean SED, with little agreement regarding the distributions of the SED relative to observation data.

The differences in model distributions have been attributed to the models tending to produce areas of cloud $\leq$ 253 K that are smaller than the associated areas of rain rates $\geq$ 4 mm hr^{-1} for each storm, particularly in the case of the 1500 m model. The combination of this behaviour with the resolution problem then served to create a very different impression of the model behaviour to that obtained using radar composite data and radar fields. This made comparison of the relationship between deep convection and rainfall in the observation data with those in the models largely ineffective when using mean and distribution statistics. Consequentially, it cannot be said to what extent the relationship found in the models is an accurate simulation of what actually took place.

The rain-cloud fraction results were not limited so severely; they clearly displayed a large reduction in the proportion of deep cloud producing rain rates $\geq$ 4 mm hr^{-1} as grid-length was reduced, and none of the literature reviewed gives reason to dispute this. It is also clear that, on average, the 1500 m model simulated heavy rain cores that were too large relative to the area of deep cloud associated with each storm. As with the mean and distribution data, the accuracy of the models relative to observations can't be truly assessed using the observation results obtained. However, in this case it was possible to see that the 500 m and 200 m models probably simulated cores that, on average, were more accurate than those of the 1500m model.

The rain-rain fractions and 'Blob Factor' analysis have produced satisfactory results that fit in with the model characteristics observed both in this study and others. Rain rates within storms simulated by the 1500 m model tended to be too high, and a reduction of grid length to 500 m did not improve the accuracy by much. The 200 m model simulated rain rates very close to those observed by the radar composite, demonstrating a good representation of cloud core structure, despite the coverage of deep cloud tending to be too low as inferred from the rain-cloud fractions. The simulated deep convection had the most blob-like appearance, with the least complex structure, in the 1500 m model, when the period of study is considered as a whole. Several times during the day, however, this 'Blob Factor' analysis revealed similar storm

characteristics to those of the 500 m and 200 m models. These two models displayed similar behaviour to one another, and were close to that of the radar for much of the time. Attempts to attribute the variation in 'Blob Factor' to changes in other storm properties did not produce any significant results, but the possibility of such relationships has not been ruled out, given that, as a consequence of time constraints, the combined size of the datasets used to calculate the 'Blob Factor' values was not very large. Results for the fraction of heavy rain occurring outside of deep cloud, and the cloud-cloud fractions, did not expand on those from other analysis, due to the impact of the resolution problem.

The extensive and at times severe impact that the resolution problem had on the results inevitably leads to the conclusion that satellite data at a close to 10 km grid length is highly inadequate observing small scale convective features. Therefore it is considered unsuitable for assessing the handling of such features by models with grid lengths of 1.5 km or less.

The fact that a few realistic results, supported by existing literature, were still obtained suggests that, if satellite data of a resolution much closer to that of high resolution models was to be used, there is the potential to produce a wide range of significant results that greatly expands upon existing studies of such models. Another promising route for further analysis is an investigation of rain-rain fractions using a range of intensity thresholds, building a more complete impression of core structure that may support the results in Stein *et al*. (2014), for example. Finally, there is evidence to suggest that the 'Blob Factor' analysis could produce interesting and informative results if applied to larger datasets to both compare models and investigate potential relationships with other storm properties, such as storm diameters and rain rates.

References

Archiv-Version des Animationstools (2014). Retrieved 7th July, 2014, from: http://www.wetter3.de/Archiv/

Atmospheric Soundings (2014). Retrieved 7th July 2014, from: http://weather.uwyo.edu/upperair/sounding.html

Battan, L.J. (1973): *Radar observation of the atmosphere.* University of Chicago Press, Chicago, USA.

Bennet, L.J., K.A. Browning, A.M. Blyth, D.J. Parker and P.A. Clark (2006): A review of the initiation of precipitating convection over the United Kingdom. *Journal of the Royal Meteorological Society*, 132 (617), p.1001-2010.

Best, M.J., M. Pryor, D.B. Clark, G.G. Rooney, R.L.H. Essery, C.B. Mènard, J.M. Edwards, M.A. Hendry, A. Porson, N. Gedney, L.M. Mercado, S. Sitch, E. Blyth, O. Boucher, P.M. Cox, C.S.B. Grimmond and R.J. Harding (2011): The Joint UK Land Environment Simulator (JULES), model description – Part 1: Energy and water fluxes. *Geosci. Model Dev.*, 4, 677-699.

Bringi, V.N., M.A. Rico-Ramirez and M. Thurai (2011): Rainfall estimation with an operational polarimetric c-band radar in the United Kingdom: Comparison with a gauge network and error analysis. *Journal of Hydrometeorology*, 12, 935-954.

Browning, K.A., A.M. Blyth, P.A. Clark, U. Corsmeier, C.J. Morcrette, J.L. Agnew, S.P. Ballard, D., Bamber, C. Barthlott, L.J. Bennett, K.M. Beswick, M. Bitter, K.E. Bozier, B.J. Brooks, C.G. Collier, F. Davies, B. Deny, M.A. Dixon, T. Feuerle, R.M. Forbes, C. Gaffard, M.D. Gray, R. Hankers, T.J. Hewison, N. Kalthoff, S. Khodayar, M. Kohler, C. Kottmeier, S. Kraut, M. Kunz, D.N. Ladd, H.W. Lean, J. Lenfant, Z. Li, J. Marsham, J. McGregor, S.D. Mobbs, J. Nicoli, E. Norton, D.J. Parker, F. Perry, M. Ramatschi, H.M.A. Ricketts, N.M. Roberts, A. Russel, H. Schulz, E.C. Slack, G. Vaughan, J. Waight, R.J. Watson, A. R. Webb, D.P. Wareing and A. Wieser (2007): The Convective Storm Initiation Project. *Bulletin of the American Meteorological Society*, 88(12), 1939-+.

Browning, K.A. and N.M. Roberts (1994): Use of satellite imagery to diagnose events leading to thunderstorms: Part 1 of a case-study. *Meteorological Applications*, 1, 303-310.

Browning, K.A. and G.A. Monk (1982): A simple model for the synoptic analysis of cold fronts. *Quarterly Journal of the Royal Meteorological Society*, 108, 435-452.

Browning, K.A. (1978): The structure and mechanisms of hailstorms. *Meteorological Monogr.*, 38, 1-43.

Bryan, G.H. and R. Rotunno (2005): Satistical convergence in simulated moist absolutely unstable layers. Preprints, *11th Conference on Mesoscale Processes*, Albuquerque, N.M., American Meteorological Society, 1M.6.

Burt, S. (2005): Cloudburst upon Hendraburnick Down: the Boscastle Storm of 16 August 2004. *Weather*, 60, 219-227.

Burt, T. and S. Lane (2008): Extreme UK Floods. *Geography Review*, 22(2), 2-5.

Crook, N.A. (1996). Sensitivity of moist convection forced by boundary-layer processes to low-level thermodynamic fields. *Monthly Weather Review*, 124, 1767-1785.

Cullen, M.J.P., T. Davies, M.H. Mawson, J.A. James, S.C. Coulter and A. Malcolm (1997): An overview of numerical methods for the next generation UK NWP and climate model. *Numerical Methods in Atmospheric and Ocean Modelling: The André J. Robert Memorial Volume,* C.A. Lin, R. Laprise and H. Ritchie (Eds.), Canadian Meteorological and Oceanographic Society, 425-444.

Davies, T., M.J.P. Cullen, A.J. Malcolm, M.H. Mawson, A. Staniforth, A.A. White and N. Wood (2005): A new dynamical core for the Met Office's global and regional modelling of the atmosphere. *Quarterly Journal of the Royal Meteorological Society*, 131, 1759-1782.

Done, J., C.A. Davis and M. Weisman (2004): The next generation of NWP: Explicit forecasts of convection using the weather research and forecasting (WRF) model. *Atmospheric Science Letters*, 5, 110-117.

Edwards, J. and A. Slingo (1996): Studies with a flexible new radiation code. Part 1: Choosing a configuration for a large-scale model. *Quarterly Journal of the Royal Meteorological Society*, 122, 689-719.

Farnborough Hourly Weather History and Observations (2014). Retrieved 7th July 2014, from: http://www.wunderground.com/history/airport/EGLF/2012/8/25/DailyHistory.html?req_city =Reading&req_state=&req_statename=United+Kingdom.

Futyan, J.M. and A.D. Del Genio (2007): Deep convective system evolution over Africa and the Tropical Atlantic. *Journal of Climate*, 20, 5041-5060.

Garner, S.T. and A.J. Thorpe (1992): The development of organized convection in a simplified squall-line model. *Quarterly Journal of the Royal Meteorological Society*, 118, 101-124.

Gunn, K.L.S. and T.W.R. East (1954): The microwave properties of precipitation particles. *Quarterly Journal of the Royal Meteorological Society*, 80, 522-545. DOI: 10.1002/qj.49708034603.

Halliwell, C. (2007). 'Subgrid turbulence scheme', Unified Model Documentation Paper 28. Met Office: Exeter, UK.

Hand, W.H., N.I. Fox and C.G. Collier (2004): A study of twentieth-century extreme rainfall events in the United Kingdom with implications for forecasting. *Meteorological Applications*, 11, 15-31.

Hanley, K.E., R.S. Plant, T.H.M. Stein, R.J. Hogan, J.C. Nicol, H.W. Lean, C. Halliwell and P.A. Clark (2014): Mixing-length controls on high-resolution simulations of convective storms. *Quarterly Journal of the Royal Meteorological Society*. doi: 10.1002/qj.2356

Haralick, R.M.; and L.G. Shapiro (1992*): Computer and Robot Vision (Volume I)*. Michigan: Addison-Wesley Pub. Co., 39-46.

Hardy, K.R. and H. Ottersten (1969): Radar investigation of convective patterns in the clear atmosphere. *Journal of Atmospheric Science*, 26, 666-672.

Harrison DL, Norman K, Pierce C, Gaussiat N. 2011. Radar products for hydrological applications in the UK. *Proceedings of the Institution of Civil Engineers* 165: 89–103. DOI: http://www.icevirtuallibrary.com/content/article/10.1680/wama.2012.165.2.89

Harrison, D., R. Scovell and M. Kitchen (2009): High-resolution precipitation estimates for hydrological uses. *Proc. ICE – Water Management*, 162, 125-135.

Hohenegger, C., and C. Schar (2007): Atmospheric predictability at synoptic versus cloud-resolving scales. *Bulletin. American Meteorological Society,* **88,** 1783–1793.

Houze, R.A., Jr. and E.N. Rappaport (1984): Air motions and precipitation structure of an early summer squall line over the eastern tropical Atlantic. *Journal of Atmospheric Science*, 41, 553-574.

Lean, H.W., P.A. Clark, M. Dixon, N.M. Roberts, A. Fitch, R. Forbes, and C. Halliwell (2008): Characteristics of high-resolution versions of the Met Office Unified Model for forecasting convection over the United Kingdom. *Monthly Weather Review*, 136, 3408-3424. Doi: 10.1175/2008MWR232.1.

Lorenz, E.N. (1969): Atmospheric predictability as revealed by naturally occurring analogues. *Journal of Atmospheric Science*, 26, 636-646.

Marhall, J., W. Hitschfeld and K. Gunn (1955). *Advances in Radar Weather*. Elsevier: Amsterdam, Netherlands.

Marsham, J.H. and Parker, D.J. (2006): Secondary initiation of multiple bands of cumulonimbus over southern Britain. Part II: Dynamics of secondary initiation. *Quarterly Journal of the Royal Meteorological Society*, 132, 1053-1072.

McBeath, K., P.R. Field and R.J. Cotton (2014): Using operational weather radar to assess high-resolution numerical weather prediction over the British Isles for a cold air outbreak case-study. *Quarterly Journal of the Royal Meteorological Society*, 140, 225-239. DOI: 10.1002/qj.2123.

Mecikalski, J.R. and K.M. Bedka (2006): Forecasting Convective Initiation by Monitoring the Evolution of Moving Cumulus in Daytime GOES Imagery, *Monthly Weather Review*, 134, 49-78.

Merk, D. and T. Zinner (2013): Detection of convective initiation using Meteosat SEVIRI: implementation in and verification with the tracking and nowcasting algorithm Cb-TRAM. *Atmospheric Measuring Techniques*, 6(8), 1903-1918. DOI: 10.5194/amt-6-1903-2013.

Morcrette, C., H. Lean, K. Browning, J. Nicol, N. Roberts, P. Clark, A. Russel and A. Blyth (2007): Combination of Mesoscale and Synoptic Mechanisms for Triggering an Isolated Thunderstorm: Observational Case Study of CSIP IOP 1. *Monthly Weather Review*, 135, 3728-3749. DOI: 10.1175/2007MWR2067.1

Morcrette, C.J., K.A. Browning, A.M. Blyth, K.E. Bozier, P.A. Clark, D. Ladd, E.G. Norton and E. Pavelin (2006): Secondary initiation of multiple bands of cumulonimbus over southern Britain. Part I: An observational case study. *Quarterly Journal of the Royal Meteorological Society*, 132, 1021-1051.

Petch, J.C. (2006): Sensitivity studies of developing convection in a cloud-resolving model. *Quarterly Journal of the Royal Meteorological Society*, 132, 345-358.

Purdom, F.J.W. (1982): Subjective interpretation of geostationary satellite data for nowcasting. In *Nowcasting*, K.A. Browning, Ed., Academic Press, 149-166.

Roberts, N.M and H. W. Lean (2008): Scale-selective verification of rainfall accumulations from high resolution forecasts of convective events. *Monthly Weather Review,* **136,** 78–97.

Roberts, N.M. (2000): 'The relationship between water vapour imagery and thunderstorms'. Joint Centre for Mesoscale Meteorology, Internal Report No. 110, Reading, UK.

Romero, R.C., C.A. Doswell and R. Riosalido (2001): Observations and fine-grid simulations of a convective outbreak in north-eastern Spain: Importance of diurnal forcing and convective cold pools. *Monthly Weather Review*, 129, 2157-2182.

Russell, A., G. Vaughan, E.G. Norton, C.J. Morcrette, K.A. Browning and A.M. Blyth (2008): Convective inhibition beneath and upper-level PV anomaly. *Quarterly Journal of the Royal Meteorological Society*, 134(631), 371-383. DOI: 10.1002/qj.214.

Smagorinsky, J. (1963). General circulation experiments with the primitive equations. I: The basic experiment. *Monthly Weather Review*, 91, 99-164.

Speer, M.S. and L.M. Leslie (2002): The prediction of two cases of severe convection: implications for forecast guidance. *Meteorology and Atmospheric Physics*, 80, 1-4.

Stein, T.H.M., R.J. Hogan, K.E. Hanley, J.C. Nicol, H.W. Lean, R.S. Plant, P.A. Clark and C.E. Halliwell (2014): The thee-dimensional morphology of simulated and observed convective storms over southern England. *Monthly Weather Review.* DOI: http://dx.doi.org/10.1175/MWR-D-13-00372.1

Vicente, G. A., J. C. Davenport and R. A. Scofield (2002): The role of orographic and parallax corrections on real time high resolution satellite rainfall rate distribution, *International Journal of Remote Sensing*, 23:2, 221-230.

Vosper, S., E. Carter, H.W. Lean, A. Lock, P.A. Clark and S. Webster (2013): High-resolution modelling of valley cold pools. *Atmospheric Science Letters*, 14, 193-199. DOI: 10.1992/asl2.439.

Weckwerth, T.M. (2000): The effect of small-scale moisture variability on thunderstorm initiation. *Monthly Weather Review*, 128, 4017-4030.

Weckwerth, T.M. and D.B. Parsons (2006). A review of convection initiation and motiviation for IHOP_2002. *Monthly Weather Review*, 133, 5-22.

Weisman, M.L., W.C. Skamarock and J.B. Klemp (1997): The resolution dependence of explicitly modelled convective systems. *Monthly Weather Review*, 125, 527-548.

Wilson, D.R. and S.P. Ballard (1999): A microphysically based precipitation scheme for the UK Meteorological Office Unified Model. *Quarterly Journal of the Royal Meteorological Society*, 125, 1607-1636.

Appendix A.

Differences to Radar Frequencies for Storm Equivalent Diameters Derived from Rainfall Data

Rainfall Data:
DRF: STORM EQUIVALENT DIAMETER (km)

1500m Time (UTC)	Small (3-10km)	Medium (10-15km)	Large (15-25km)		500m Time (UTC)	Small (3-10km)	Medium (10-15km)	Large (15-25km)		200m Time (UTC)	Small (3-10km)	Medium (10-15km)	Large (15-25km)
1000	-50	-8	5		1000	-42	-9	13		1000	50	23	16
1100	-69	-28	2		1100	-42	-4	31		1100	38	14	22
1200	-79	-26	-2		1200	-59	2	37		1200	48	36	18
1300	-55	-24	2		1300	-23	5	39		1300	109	33	31
1400	-81	-42	-8		1400	-41	-25	26		1400	43	-7	13
1500	-63	-39	0		1500	-36	-12	25		1500	23	-8	9
1600	-72	-33	0		1600	-52	-29	23		1600	-15	-23	-3
1700	-73	-31	1		1700	-37	-26	16		1700	-28	-24	-2
1800	-51	-47	-2		1800	-36	-35	18		1800	-25	-41	-2
1300	-53	-23	-3		1900	-40	-10	8		1900	-27	-8	-2
###	-25	-11	-5										
2100	-18	-5	-3										
###	-10	-6	1										

More Than 60	-30 to -60	-30 to -10	-10 to +10	+10 to +30	+30 to +60	More Than +60

Appendix B.

Distributions of Storm Areas in the 500m Model 1000-1900 UTC

500m

Time (UTC)															
1000	5	15	10	7	5	4	4	1	0	0	0	1	0	0	0
1100	12	20	17	17	15	15	5	5	2	1	1	0	0	0	0
1200	12	31	24	20	28	31	13	6	1	1	0	0	0	0	0
1300	26	39	47	41	40	20	16	7	5	0	0	0	0	0	0
1400	33	71	60	44	51	31	21	13	5	1	0	1	0	1	0
1500	47	58	73	58	46	43	32	17	12	4	5	0	1	1	0
1600	51	101	85	57	60	45	37	23	16	5	1	0	0	0	0
1700	38	74	62	65	48	47	33	13	8	4	4	1	0	0	1
1800	37	69	55	52	48	34	22	11	15	8	5	1	0	0	0
1900	36	62	53	40	34	19	18	9	6	3	3	2	1	0	0

1724 Less than 10km^2 | *1097 More than 10km^2*

Storm Area (km^2)